UNIVERSITY OF OKLAHOMA

GRADUATE COLLEGE

ENHANCING THERMAL CONDUCTIVITY OF EPOXY/GRAPHENE COMPOSITES THROUGH FILLER DISPERSION, EXPANDED GRAPHITE NETWORKS, AND 3D PRINTING

A DISSERTATION

SUBMITTED TO THE GRADUATE FACULTY

in partial fulfillment of the requirements for the

Degree of

DOCTOR OF PHILOSOPHY

By

SWAPNEEL DANAYAT

Norman, Oklahoma

2026

Downloaded from SHAREOK. Persistent Handle URL: https://hdl.handle.net/11244/342855

ENHANCING THERMAL CONDUCTIVITY OF EPOXY/GRAPHENE COMPOSITES THROUGH FILLER DISPERSION, EXPANDED GRAPHITE NETWORKS, AND 3D PRINTING

A DISSERTATION APPROVED FOR THE SCHOOL OF AEROSPACE AND MECHANICAL ENGINEERING

BY THE COMMITTEE CONSISTING OF

Dr. Jivtesh Garg, Chair

Dr. Yingtao Liu

Dr. Wilson Merchan-Merchan

Dr. Hanping Ding

Dr. Liangliang Huang

© Copyright by SWAPNEEL DANAYAT 2026
All Rights Reserved.

Acknowledgements

I would first like to express my sincere gratitude to my Ph.D. advisor, Dr. Jivtesh Garg, for giving me the opportunity to pursue research in this field and for his guidance throughout my doctoral studies. His support, feedback, and direction were important at every stage of my Ph.D., from developing research ideas to conducting experiments, analyzing results, and preparing this dissertation. I am also grateful to my dissertation committee members, Dr. Yingtao Liu, Dr. Wilson Merchan-Merchan, Dr. Hanping Ding, and Dr. Liangliang Huang. I am honored that they believed in my ability to conduct independent research, and I sincerely appreciate their time, commitment, constructive feedback, and valuable discussions during my Ph.D.

I would like to thank everyone who assisted me with experimental characterization and research support. I am grateful to Dr. Tingting Gu for assisting with and conducting the confocal microscopy imaging. Her guidance was very helpful in understanding the imaging process and image analysis. I would also like to thank Dr. Preston Larson and Zarin Tasnim Mona for their assistance with SEM imaging. I gratefully acknowledge Dr. Jacob John, Dr. Steven Michalski, Ather Mahmood, and the Nebraska Nanoscale Facility for conducting the XRD and XPS measurements used in this research.

I am thankful to Dr. Fatema Tarannum and Dr. Rajmohan Muthaiah, senior members from my lab, for helping me settle into the research environment. I would also like to thank my friends and lab colleagues, Avinash Nayal, Roshan Sameer Annam, and Zarin Tasnim Mona, for their assistance with various laboratory processes and for the many research discussions we had during my Ph.D. Brainstorming with them helped me improve my understanding, develop new ideas, and approach experiments from different perspectives.

I would also like to express my sincere appreciation to Dr. Farrokh Mistree, faculty mentor for the Graduate Student Committee, for helping me in many different aspects of my Ph.D. His guidance helped me improve my presentation skills, communication skills, and overall professional development. I am also grateful to Dr. Ramkumar Parthasarathy, Chair of the School of Aerospace and Mechanical Engineering, and to Aaron Henly, Samarpita Ghosh, and Kyle Packer from the school's administrative staff. Their assistance with administrative matters, teaching assistantship-

related work, financial matters, and other necessary processes helped me complete my Ph.D. without serious difficulties. I would also like to thank Greg Williams and Billy Mays from the school's machine shop for their immense help with the logistical, fabrication, and machining work required for multiple experimental setups. I would like to respectfully remember Billy Mays, who passed away last November, and express my gratitude for his kindness, support, and contributions to my work.

Finally, I would like to thank the friends who made my life at the University of Oklahoma meaningful and memorable. I am especially grateful to Mayank Bhalerao, who was always there whenever I needed support. Our coffee sessions led to many meaningful discussions about research and life, and I truly appreciate his help during the final stages of my Ph.D., especially while completing my dissertation writing and preparing for my defense presentation. I would also like to thank Vishnu Kadiyala, Trupti Chaure, Shravan Saoji, Maya Verma, Badal Bhalla, Sakshi Bahamnia, and all the other friends who have been and continue to be an important part of my life at OU. They became like a family to me away from home, and our game nights, late-night research discussions, and many other shared activities helped me stay motivated throughout this journey. Most importantly, I express my deepest gratitude to my parents, Shailesh Danayat and Sandhya Danayat, whose constant support, encouragement, and motivation have been the foundation of my journey. Their belief in me helped me move forward through the challenges of graduate school, and this accomplishment would not have been possible without their love and support.

Abstract

Modern thermal management systems require materials which are low weight, flexible in processing, durable, cost effective and highly thermally conductive. Polymers like epoxy are a good candidate by having all the essential properties except one – high thermal conductivity. The low intrinsic thermal conductivity of epoxy limits its direct use in modern thermal management applications. Adding highly thermally conductive fillers to polymers is considered as a strong method to prepare composite materials. Thermally conductive composites, if processed right, can have high thermal conductivity while also retaining the intrinsic properties of polymers to make them suitable for modern thermal management systems. Among multiple filler materials studied, graphene nanoplatelets are particularly promising. Although, translating the high thermal conductivity of graphene into a high thermal conductivity composite material is extremely challenging. The presented work addresses three of these challenges – graphene agglomeration at low concentrations, high filler-filler contact resistance and filler-matrix interfacial resistance, and anisotropic thermal conductivity of graphene with multifold higher in-plane thermal conductivity than through-plane. This dissertation investigates three processing-based strategies to enhance the thermal conductivity of epoxy/graphene-based composites by controlling filler dispersion, graphitic network connectivity, and filler alignment.

The first study addresses the first challenge of efficient graphene dispersion in epoxy matrix by comparing two solvents – dimethylformamide (DMF) and acetone, used as processing solvents to mix epoxy and the graphene fillers. To focus on the dispersion aspect, this study was performed at low graphene loadings of 3, 5 and 7wt%. Results showed that the composite samples made with DMF as a solvent showed 40% and 44% higher thermal conductivity than samples made with acetone at 5wt% and 7wt% respectively. Laser Scanning Confocal Microscopy (LSCM)

was used to analyze and compare the graphene dispersion in these samples. LSCM images showed that acetone-based samples contained large graphene-rich agglomerates, whereas DMF-based samples exhibited uniform distribution of the graphene nanoplatelets. Further analysis of these images showed that the maximum agglomerate volumes in acetone-based samples were 211% and 93% higher than DMF-based samples at 5wt% and 7wt% respectively. Using effective medium theory, the apparent interfacial thermal resistance of DMF-based samples was found to be approximately 45% lower than the acetone-based samples, thus confirming the improved dispersion of graphene nanoplatelets in the composite.

The second study addresses the second challenge of filler connectivity within the composite material by using expanded graphite (EG) as a filler. To prepare the expanded graphite filler, -10 mesh graphite flakes were first intercalated using hydrogen peroxide and sulfuric acid as intercalating agents to obtain graphite intercalated compounds (GICs). These GICs were then thermally expanded around 900 °C to obtain expanded graphite. A reaction time optimization was conducted to find the highest epoxy/EG composite through-plane thermal conductivity at 10wt% EG loading. The optimized H_2O_2-derived expanded graphite produced a substantial increase in epoxy thermal conductivity, reaching a maximum value of 5.15 W m^{-1} K^{-1} at 10wt% filler loading. This enhancement is attributed to the ability of expanded graphite to form more continuous graphitic pathways within the epoxy matrix, thereby reducing the dependence on many discrete filler-filler contacts. However, higher filler loadings of 12.5 and 15wt% showed reduced thermal conductivity due to poor composite structural integrity, insufficient epoxy bonding, and weaker filler-filler contact quality. Raman, XPS, XRD analysis were performed to characterize the EG fillers. FE-SEM imaging was used to check the structural morphology of the fillers.

The third study focuses on the third challenge of filler alignment. Paste extrusion 3D printing was investigated as a processing route to improve the in-plane directional thermal conductivity of epoxy/graphene composites. An 80 mm long rectangular opening nozzle was used to print rectangular shaped epoxy composite samples with 9wt% graphene loading and the effect of printing speed on thermal and electrical conductivity along the printing direction was evaluated. Angstrom method and four-probe method were used for thermal conductivity and electrical conductivity measurements respectively. Increasing the printing speed from 750 mm/min to 1500 mm/min resulted in approximately 27% higher thermal conductivity and 106% higher electrical conductivity along the print direction. These results indicate that printing speed can influence the effectiveness of the graphitic network, likely through changes in filler orientation and filler connectivity.

Overall, this dissertation demonstrates that thermal conductivity enhancement in epoxy/graphene-based composites is controlled not only by filler loading, but also by the internal organization of graphitic fillers within the epoxy matrix. Improved dispersion, expanded graphite network formation, and 3D-printing-induced alignment provide complementary approaches for improving thermal transport in lightweight epoxy-based composites for thermal management applications.

Keywords: Thermal conductivity, graphene, polymer composites, epoxy, 3d printing, dispersion, agglomeration, alignment, intercalation

Table of Contents

Abstract		vi
Table of Contents		ix
List of Figures		xi
Chapter 1	Introduction	1
1.1	Challenges and Research Objectives	3
1.2	Outline of the Dissertation	5
Chapter 2	Enhancement of Epoxy/Graphene Composite Thermal Conductivity Through Improved Graphene Dispersion	8
2.1	Introduction	8
2.2.1	Materials	13
2.2.2	Epoxy-GnP Composite Sample Preparation	13
2.2.3	Measurements and Characterization	15
2.3	Results and Discussion	17
2.4	Conclusions	24
Chapter 3	Enhancement of Epoxy Composites Using Expanded Graphite	27
3.1.1	Introduction	27
3.1.2	Graphite Intercalated Compounds	32
3.2.1	Materials	35
3.2.2	H_2O_2/H_2SO_4 Intercalation Process and Synthesis of EG	35
3.2.3	Preparation of Epoxy/Expanded Graphite Composite Samples	38
3.2.4	Measurements and Characterization	40
3.3	Results and Discussion	43
3.3.1	Reaction Time Optimization Study for H_2O_2-Based EG Intercalation	43
3.3.2	Raman Analysis	48
3.3.3	X-ray Photoelectron Spectroscopy Analysis	52

3.3.4	X-ray Diffraction Analysis	56
3.3.5	GIC and EG Structure and Morphology	61
3.4	Conclusion	62
Chapter 4	Enhancement of Epoxy/Graphene Through Graphene Alignment Using 3D Printing	65
4.1	Introduction	65
4.2	Materials and Experimental Methods	67
4.3	Angstrom Method for In-Plane Thermal Conductivity Measurement	72
4.4	Results and Discussion	76
4.5	Conclusions	79
Chapter 5	Conclusions	81
—	References	87

List of Figures

Figure 2.1 Schematic for sample preparation…… 14
Figure 2.2 Thermal conductivity of graphene/epoxy composites prepared using two different solvents with increasing graphene concentration…… 19
Figure 2.3 Confocal microscopy images for acetone-based samples for concentrations a) 3wt%, b) 5wt%, c) 7wt% and DMF-based samples for concentrations d) 3wt%, e) 5wt%, f) 7wt%..... 20
Figure 2.4 Graphene suspension in acetone and DMF at t = 0, 5 and 24 hours…… 22
Figure 2.5 a) Maximum graphene agglomeration volume comparison, b) Effective medium theory and measured thermal conductivity values……. 24
Figure 3.1 Enhancement in thermal conductivity for different EG/Epoxy composites…… 29
Figure 3.2 Diagram depicting the preparation process of graphite intercalation compounds (GIC) using acids and oxidizing agents, followed by thermal expansion to produce expanded graphite (EG)……. 33
Figure 3.3 Schematic for graphite intercalation procedure……... 37
Figure 3.4 Schematic illustration for preparation technique of epoxy/EG composite…….. 39
Figure 3.5 Optical images of half-inch circular Epoxy-EG samples prepared for thermal diffusivity measurements……... 40
Figure 3.6 Optimization of reaction time for thermal diffusivity enhancement of epoxy/EG composites (H_2SO_4:H_2O_2 = 4:1)…… 44
Figure 3.7 Epoxy/EG composite thermal conductivities (k) values at 5, 7.5, 10, 12.5, 15wt% filler concentration……. 47
Figure 3.8 Raman survey spectra of a) GIC and b) EG fillers synthesized during reaction-time optimization for epoxy/EG composite study…….. 48
Figure 3.9 XPS survey spectra of a) EG and b) GIC fillers synthesized during reaction-time optimization for epoxy/EG composites, showing characteristic C 1s (~285 eV) and O 1s (~532 eV) peaks……. 52
Figure 3.10 XPS survey spectra of a) EG and b) GIC fillers synthesized during reaction-time optimization for epoxy/EG composites, showing characteristic C 1s (~285 eV) and O 1s (~532 eV) peaks……. 56
Figure 3.11 Inset of XRD spectra of a) EG and b) GIC samples showing peak broadening and shifting in the (002) reflection during reaction-time optimization for epoxy/EG composites…….. 57
Figure 3.12 FE-ESEM images of 10 mesh graphite a) 35X and b) 150X and FE-ESEM micrographs of the optimized expanded graphite (SD-H4 EG) used in the epoxy/EG composite, captured at various magnifications: (c) 50×, (d) 150×, (e) 1000×, (f) 86×, (g) 350×, and (h) 1000×……... 60
Figure 4.1 FELIX food 1.6 single head 3-d printer……... 66
Figure 4.2 Visual representation of G-code in Simplify3D software…… 67
Figure 4.3 Nozzle used to print the epoxy/GnP samples…….. 68

Figure 4.4 3D printed sample with attached heating wire……. 69
Figure 4.5 Angstrom method setup for in-plane thermal diffusivity measurement…….. 70
Figure 4.6 Sample holder for 3D printed samples……. 72
Figure 4.7 Screenshot of FLIR ResearchIR Max software during measurement……. 73
Figure 4.8 In-plane thermal and electrical conductivity of 3D printed epoxy/GnP sample….. 77

Chapter 1

Introduction

Rapid growth in electronic devices, electric vehicles, battery systems, power electronics, and compact energy systems has increased the need for materials that can dissipate heat efficiently. As device dimensions decrease and power densities increase, heat generated during operation becomes more difficult to remove. Poor heat dissipation can increase operating temperature, reduce device efficiency, accelerate material degradation, and eventually cause component failure. Traditionally, metals such as copper and aluminum have been widely used for heat spreading and heat dissipation because of their high thermal conductivity. However, metallic thermal management systems can be limited by high density, corrosion susceptibility, electrical conductivity, processing difficulty for complex geometries, and reduced suitability for applications where lightweight and electrically insulating materials are required. These limitations have created a need for alternative thermal management materials that combine improved thermal conductivity with low weight, electrical insulation, corrosion resistance, and processability.

Polymers are attractive materials for many engineering applications because they are lightweight, low cost, chemically stable, corrosion resistant, electrically insulating, and easy to process into complex shapes[1-3]. Epoxy is particularly useful because of its good mechanical strength, adhesion, chemical resistance, and processability. These advantages make epoxy suitable for applications such as adhesives, coatings, encapsulation, electronic packaging, and composite matrices. However, the major limitation of epoxy and most other polymers is their low intrinsic thermal conductivity, typically in the range of ~0.1–0.5 $Wm^{-1}K^{-1}$. This low thermal conductivity restricts their direct use in applications where rapid heat dissipation is required[4-6]. Therefore, a

common approach is to incorporate high thermal conductivity fillers into the polymer matrix to form thermally conductive polymer composites[7-10]. These composites can retain several advantages of polymers while providing improved heat transfer performance.

Graphene-based and graphite-based fillers have been widely studied for improving the thermal conductivity of polymer composites. Graphene has extremely high in-plane thermal conductivity, with reported values in the range of ~2000–5000 $Wm^{-1}K^{-1}$, which makes it a promising filler for thermal transport enhancement[7,11,12]. Graphene nanoplatelets (GnPs), graphite, and expanded graphite are especially useful because they can form thermally conductive pathways inside the polymer matrix[13-16]. Incorporation of these fillers into epoxy can increase the effective thermal conductivity of the composite while preserving many of the advantages of the polymer, such as low density, corrosion resistance, and processability. Because of this combination of properties, epoxy/graphene-based composites are promising materials for lightweight thermal management applications[17,18].

However, the high intrinsic thermal conductivity of graphene does not automatically result in high thermal conductivity of the final composite. The effective thermal conductivity of epoxy/graphene composites depends strongly on the distribution, contact, and orientation of graphitic fillers inside the epoxy matrix[8,10,19]. Graphene nanoplatelets tend to agglomerate because of strong van der Waals interactions, which can lead to non-uniform dispersion and ineffective thermal pathways[1,10,20-22]. Heat transfer in the composite is also limited by thermal interface resistance between the filler and the matrix and thermal contact resistance between neighboring fillers[23-25]. In addition, graphene has highly anisotropic thermal conductivity, with much higher thermal conductivity along the in-plane direction than through the thickness direction[26,27]. Random orientation of GnP in the composite limits the use of this high in-plane thermal conductivity. This

dissertation focuses on improving the thermal conductivity of epoxy/graphene-based composites by addressing these three limitations through improved dispersion of GnP, thermal expansion of graphite, and 3D-printing-induced alignment of GnP.

1.1 Challenges and Research Objectives

The thermal conductivity of epoxy/graphene-based composites is governed not only by the intrinsic thermal conductivity of the graphitic filler, but also by the structure of the filler network formed inside the epoxy matrix[28,29]. For heat to move efficiently through the composite, graphitic fillers must be well distributed, thermally connected, and oriented in directions that support the desired heat flow. In practice, achieving these conditions is difficult because graphene-based fillers introduce several processing and transport challenges. In this dissertation, three major challenges are considered: agglomeration of graphene nanoplatelets, thermal resistance at filler-polymer and filler-filler contacts, and the highly anisotropic thermal conductivity of graphene. The research objectives of this dissertation are designed to address these limitations by controlling the dispersion, connectivity, and orientation of graphitic fillers in epoxy composites.

The first challenge is the agglomeration of graphene nanoplatelets within the epoxy matrix. As mentioned previously, Graphene sheets and graphene nanoplatelets tend to reaggregate because of strong van der Waals forces between them. This reaggregation leads to non-uniform dispersion, where some regions of the composite contain large graphene-rich agglomerates while other regions contain insufficient filler. Such non-uniform dispersion limits the formation of efficient thermal pathways through the polymer matrix and reduces the effective contact area between graphene and epoxy. Uniform dispersion of graphene is therefore important for achieving high thermal

conductivity in epoxy/graphene composites. One simple and effective route to improve dispersion is the use of organic solvents that can stabilize graphene sheets before incorporation into the epoxy matrix. Solvent selection can influence the stability of graphene dispersions, the extent of reaggregation during processing, and the final morphology of the cured composite[21,22]. Therefore, the first objective of this dissertation is to improve the dispersion of graphene nanoplatelets in epoxy composites by comparing dimethylformamide (DMF) and acetone as processing solvents and evaluating their effect on agglomeration, interface resistance, and thermal conductivity. This objective forms the basis of Chapter 2.

The second challenge is the presence of thermal resistance at interfaces and contacts inside the composite. Heat conduction in epoxy/graphene composites occurs through the epoxy matrix, through the graphitic fillers, and across the interfaces between them. Because of the mismatch in vibrational properties between graphene and epoxy, phonon scattering at the filler-polymer interface can reduce heat transfer across the composite[19,23,24]. In addition, heat transfer between neighboring graphene particles is limited by thermal contact resistance at graphene-graphene junctions[8,20,29]. This limitation becomes especially important when the filler network is formed by discrete graphene nanoplatelets, where heat must pass through many particle-particle contacts. A strategy to reduce the effect of these discrete contact limitations is to use expanded graphite. Expanded graphite is obtained by intercalating graphite flakes followed by rapid thermal expansion, producing graphitic structures with larger surface area and more continuous pathways compared to individual graphene nanoplatelets[13,14,30,31]. These expanded structures can help form a more connected graphitic network within the epoxy matrix, thereby improving heat transfer through the composite. Therefore, the second objective of this dissertation is to improve graphitic filler connectivity in epoxy composites through graphite intercalation and thermal expansion, and

to investigate how expanded graphite structure affects composite thermal conductivity. This objective is addressed in Chapter 3.

The third challenge arises from the anisotropic nature of graphene thermal conductivity. Graphene has much higher thermal conductivity along its in-plane direction than through its thickness direction. This means that filler orientation becomes an important factor in determining composite thermal conductivity. Naturally, in randomly oriented composites, graphene nanoplatelets are not aligned with the desired heat flow direction, which prevents full utilization of graphene's high in-plane thermal conductivity. Alignment of graphene nanoplatelets provides a way to take advantage of this anisotropy by orienting the high-conductivity direction along the direction of heat transport. In this dissertation, 3D printing is used as a processing route to induce alignment of graphene nanoplatelets in epoxy-based composites. During extrusion through the nozzle, graphene nanoplatelets can preferentially orient along the printing direction, resulting in directional filler networks[32]. Therefore, the third objective of this dissertation is to utilize 3D-printing-induced alignment of graphene nanoplatelets and investigate its effect on directional thermal transport in epoxy/graphene composites. This objective is addressed in Chapter 4.

1.2 Outline of the Dissertation

This dissertation is organized into four main chapters along with Chapter 1 which introduces the motivation for developing thermally conductive epoxy/graphene-based composites and discusses the major challenges that limit thermal conductivity enhancement in these materials and Chapter 5 which summarizes the findings of this dissertation.

Chapter 2 investigates the effect of solvent selection on the dispersion of graphene nanoplatelets in epoxy composites. Epoxy/graphene composites prepared using dimethylformamide (DMF) and acetone are compared to understand how solvent-assisted dispersion affects graphene agglomeration, thermal interface resistance, and composite thermal conductivity. Laser scanning confocal microscopy is used to characterize graphene dispersion, and effective medium theory is used to relate the observed thermal conductivity values to interface resistance.

Chapter 3 focuses on the use of thermally expanded graphite to improve graphitic filler connectivity in epoxy composites. Graphite intercalation and thermal expansion are used to prepare expanded graphite fillers. The effect of intercalation chemistry and expanded graphite structure on thermal conductivity is investigated through thermal measurements and material characterization. This chapter examines how expanded graphite can form more continuous graphitic pathways within the epoxy matrix.

Chapter 4 investigates 3D printing as a processing route to induce alignment of graphene nanoplatelets in epoxy-based composites. Paste-extrusion-based printing is used to study the effect of nozzle geometry and printing conditions on filler alignment and directional thermal transport. This chapter evaluates whether printing-induced orientation can improve the utilization of graphene's high in-plane thermal conductivity.

Chapter 5 summarizes the findings of this dissertation and discusses how the three processing approaches contribute to improved understanding of thermal transport in epoxy/graphene-based composites. The chapter also presents conclusions based on the

relationships between processing, filler structure, and thermal conductivity developed throughout this work

Chapter 2

Enhancement of Epoxy/Graphene Composite Thermal Conductivity Through Improved Graphene Dispersion

2.1 Introduction

Chapter 1 identified three major factors that limit the thermal conductivity enhancement of epoxy/graphene-based composites: graphene nanoplatelet agglomeration, thermal resistance at filler-polymer and filler-filler contacts, and inefficient use of graphene anisotropy due to random filler orientation. This chapter focuses on the first limitation- the dispersion of graphene nanoplatelets within the epoxy matrix. Although graphene has extremely high intrinsic thermal conductivity, its effectiveness as a thermally conductive filler depends strongly on how well it is distributed throughout the polymer[33,34]. Poor dispersion can produce graphene-rich agglomerates and graphene-poor regions, which limits the formation of continuous thermal transport pathways and reduces the effective contact area between graphene and epoxy. Therefore, improving graphene dispersion is an important first step toward increasing the thermal conductivity of epoxy/graphene composites[1,21,29].

One of the main challenges in epoxy/graphene composites is the tendency of graphene nanoplatelets to agglomerate during processing[20]. This agglomeration occurs because of strong Van Der Waals interactions between graphene sheets. Direct mechanical mixing of graphene into epoxy is often insufficient because the viscosity of epoxy restricts the movement and separation of graphene sheets. As a result, graphene nanoplatelets can form large agglomerates instead of

remaining uniformly distributed throughout the matrix. Such agglomerates can reduce the efficiency of thermal transport in multiple ways. First, they decrease the effective graphene-epoxy interfacial contact area, which limits heat transfer from the polymer matrix into the high-conductivity filler. Second, they create nonuniform filler distributions, where some regions contain excess graphene while other regions contain insufficient filler for thermal pathway formation. Third, large agglomerates can interrupt the development of a well-distributed filler network. Therefore, dispersion quality is a key structural factor controlling the effective thermal conductivity of epoxy/graphene composites[21,22,29].

Solvent-assisted processing is a common approach for improving graphene dispersion before incorporation into a polymer matrix.[1-3,20] Many engineering polymers and polymer precursors can be processed in organic solvents, and these solvents can reduce mixture viscosity and help separate graphene nanoplatelets before curing. In this approach, graphene is first dispersed in a solvent, the polymer or resin is then introduced, and the solvent is subsequently removed before curing. The final composite structure depends not only on the graphene loading and mixing procedure, but also on the ability of the solvent to stabilize graphene during processing. A suitable solvent can reduce reaggregation of graphene sheets, improve the uniformity of filler distribution, and influence the morphology of the cured composite. Therefore, solvent selection should be considered not only as a processing convenience, but also as a structure-control parameter that can affect thermal transport.

Studies have been conducted for the effect of solvents on dispersion of graphene in regards with improvement of mechanical properties[35]. However, no results have been reported for the effect of solvents on improvement of thermal conductivity. Acetone, one of the commonly used solvent for

preparing graphene-polymer composites has shown short-term stability of graphene dispersions when compared to many other organic solvents like dimethylformamide (DMF), tetrahydrofuran (THF), N-methyl-2-pyrrolidone (NMP) and ethylene glycol, which show long term stability of dispersions [36]. The improved dispersion of graphene in certain solvents compared to acetone, has been shown to also lead to improved mechanical properties such as mechanical strength. Mishra *et al.* compared the effect of three solvents (ethanol, acetone, and toluene) on the dispersion of polyhedral oligomeric silsequioxane (POSS) in epoxy and the subsequent enhancement of mechanical properties of POSS-epoxy nanocomposite[37]. They found that composite prepared using ethanol showed increase in elastic modulus and fracture toughness values due to the better dispersion of POSS in epoxy resin in ethanol solvent.

Wang *et al.* prepared graphene nanoplatelet/epoxy samples using acetone with 0.45 $Wm^{-1}K^{-1}$ thermal conductivity at 5wt% loading[38]. Guo *et al.* demonstrated a thermal conductivity close to 0.3 and 0.45 $Wm^{-1}K^{-1}$ for graphene/epoxy composite samples made with acetone at 5wt% and 10wt% respectively[39]. S Han *et al.* showed thermal conductivity of 0.33 $Wm^{-1}K^{-1}$ for epoxy/graphene nanoplatelets at 4wt% loading prepared using acetone[17]. While the above studies addressed the effect of improved dispersion in certain solvents on mechanical properties like mechanical strength, the present study focuses on the effect of solvents on thermal conductivity.

The dispersion capability of a solvent can be inferred from their 'Hansen Solubility Parameters' (HSP). These parameters include a dispersion cohesion parameter (δ_d), polarity cohesion parameter (δ_p) and a hydrogen bonding cohesion parameter (δ_h)[40]. For good dispersion of graphene in any solvent, it is essential that the solvent-graphene interaction is strong enough to overcome or balance than the graphene-graphene Van der Waals interaction. The three HSP parameters determine how the solvent molecules interact with other solvent molecules and any

other surface in contact[41]. S. Park *et al.* showed that highly reduced graphene (HRG) was well dispersed in solvent mixtures (DMF/H_2O mixed with either acetone, acetonitrile, THF, DMF, NMP, DMSO and ethanol) having the sum $\delta_p+\delta_h$ in the range of 13~29. They further showed that the solvent having the sum lower than 10 (DMF/H_2O mixed with either DCB, diethyl ether and toluene) and higher than 30 (water) exhibit poor dispersion of HRG[42]. The HSP sum ($\delta_p+\delta_h$) of acetone and DMF are 17.4 and 25 respectively, implying they both are viable candidates for dispersing HRG[43].

Another important parameter related to dispersion is the zeta potential (ς). Zeta potential is the electric potential difference between the dispersion medium and the stationary layer of fluid attached to the dispersed particle[44]. When a particle is dispersed in a fluid, an electrical double layer is created. The first layer comes from the charged particle surface and the second layer comes from the surrounding fluid with opposite charges. When two such particles having same charge approach each other, their charged double layer repels each other. This repulsion is denoted using a numerical value with a positive or negative sign depending on the particle charge[45,46]. A strong positive or negative zeta potential result in high repulsive forces between the dispersed particles, indicating good stability of dispersions[47]. A. A. S. Ghazvini *et al.* have shown that the zeta potential for graphene in acetone is -22.6 mV[48]. S. Gambhir *et al.* have shown that graphene in different forms has zeta potential lower than -30mV in DMF[49]. These values suggest a stronger negative zeta potential of graphene in DMF which leads to better stability of the dispersion over time. Villar-Rodil *et al.* have demonstrated stable suspension of unreduced and chemically reduced graphene in DMF over several months[50].

Previous work on solvent effects have mainly focused on dispersion behavior or mechanical property enhancement. However, comparatively less attention has been given to how solvent selection affects thermal conductivity in epoxy/graphene composites. This is an important gap because the requirements for improving thermal transport are not identical to those for improving mechanical properties. For thermal conductivity enhancement, the filler must not only be dispersed, but also arranged in a way that allows heat to move efficiently through the composite. Uniform dispersion can improve filler-polymer contact and reduce large agglomerates, but it must also support the development of thermally effective pathways across the epoxy matrix. Therefore, studying the effect of solvent-assisted dispersion on thermal conductivity provides useful insight into how processing controls heat transfer in epoxy/graphene composites.

In this chapter, acetone and DMF are compared as processing solvents for epoxy/graphene nanoplatelet composites. Graphene loadings of 3wt%, 5wt%, and 7wt% are investigated to determine how solvent choice affects thermal conductivity as filler concentration increases. The working hypothesis is that DMF provides improved graphene dispersion relative to acetone, leading to smaller agglomerates, more uniform filler distribution, lower apparent thermal interface resistance, and higher composite thermal conductivity. Thermal conductivity is measured using laser flash analysis, graphene dispersion is characterized using laser scanning confocal microscopy, and effective medium theory is used to relate the measured thermal conductivity values to apparent interface resistance. Through this approach, this chapter establishes solvent-assisted dispersion as the first structure-control strategy used in this dissertation to improve thermal transport in epoxy/graphene-based composites.

2.2 Materials and Experimental Methods

2.2.1 Materials

Graphene nanoplatelets were used as the thermally conductive filler for the preparation of epoxy/graphene composites. The graphene nanoplatelets were purchased from Graphene Supermarket and had a reported thickness of approximately 3–7 nm and lateral size of approximately 5 μm. The epoxy system used in this study consisted of EPIKOTE RESIN MGS RIMR 135 and EPIKURE CURING AGENT MGS RIMH 137, both purchased from Hexion. Acetone and N,N-dimethylformamide (DMF) were used as the two processing solvents and were purchased from the University of Oklahoma chemical stock room. Three graphene loadings were investigated: 3wt%, 5wt%, and 7wt%. These loadings corresponded to 0.15 , 0.25 , and 0.35 grams of graphene nanoplatelets, respectively, for the composite batches prepared in this study.

2.2.2 Epoxy-Gnp Composite Sample Preparation

Epoxy/graphene composites were prepared using a solvent-assisted mixing route. In this approach, graphene nanoplatelets were first dispersed in the selected solvent, followed by addition of epoxy resin, solvent removal, hardener addition, molding, and curing. The same general preparation sequence was used for both acetone- and DMF-processed composites so that the effect of solvent selection on graphene dispersion and thermal conductivity could be compared. The primary differences between the two processing routes were the sonication time and the solvent-removal temperature, which were selected based on the volatility and boiling point of each solvent.

For acetone-processed samples, 0.15 g, 0.25 g, or 0.35 g of graphene nanoplatelets were dispersed in 80 mL of acetone to prepare 3wt%, 5wt%, and 7wt% epoxy/graphene composites, respectively. The graphene/acetone suspension was tip sonicated for 1 h in an ice bath to reduce heating and limit acetone evaporation during sonication. Epoxy resin was then added to the graphene/acetone suspension, and the mixture was tip sonicated for an additional 2 h in an ice bath. After sonication, the mixture was heated to 80 °C and stirred continuously using a mechanical mixer to evaporate the acetone. The mass of the mixture was monitored during this step until the required mass was reached, indicating solvent removal. The graphene/epoxy mixture was then spread on a PTFE sheet and placed in a vacuum oven at 65 °C for 15 h to further remove residual acetone. After this drying step, the curing agent was added to the graphene/epoxy mixture. The final mixture was transferred into aluminum molds and cured at 90 °C for 20 h.

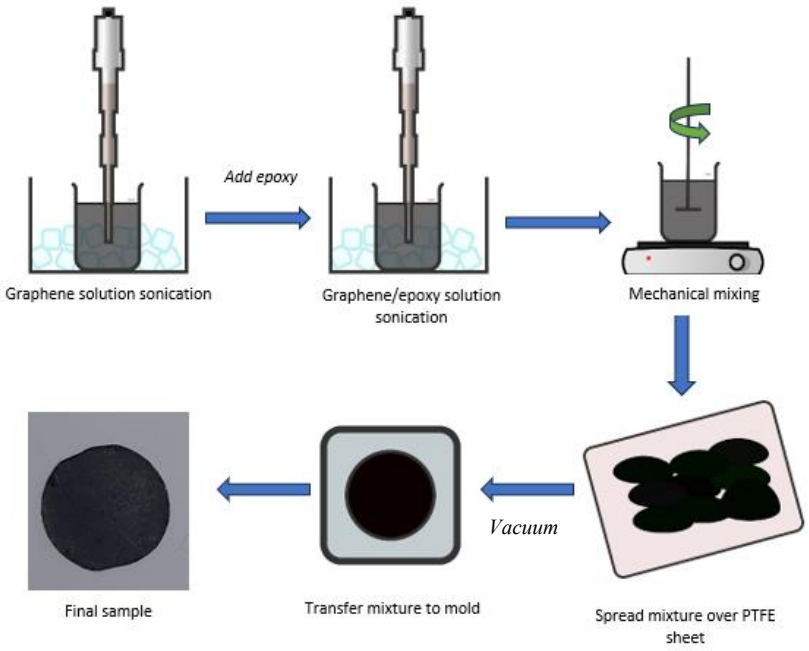


Figure 2.1 Schematic for sample preparation

For DMF-processed samples, 0.15 g, 0.25 g, or 0.35 g of graphene nanoplatelets were dispersed in 80 mL of DMF for the preparation of 3wt%, 5wt%, and 7wt% epoxy/graphene composites, respectively. The graphene/DMF suspension was sonicated in an ice bath for 30 min. Epoxy resin was then added to the suspension, and the graphene/epoxy/DMF mixture was sonicated for an additional 1 h. The mixture was then heated and mechanically stirred at 150 °C to remove DMF. Because DMF has a higher boiling point than acetone, a higher solvent-removal temperature was required for the DMF-based processing route. After mechanical mixing and solvent evaporation, the graphene/epoxy mixture was spread on a PTFE sheet and placed in a vacuum oven at 140 °C for 15 h to ensure further removal of DMF. The curing agent was then added to the dried graphene/epoxy mixture. The final mixture was transferred into aluminum molds and cured at 90 °C for 20 h. A schematic representation of the composite preparation route is shown in Figure 2.1.

2.2.3 Measurements and Characterization

Thermal conductivity of the cured epoxy/graphene composites was determined from thermal diffusivity measurements obtained using a NETZSCH LFA 467 laser flash analyzer. In the laser flash method, a short light pulse is applied to one surface of the sample, and the temperature rise on the opposite surface is recorded as a function of time using an infrared detector. The thermal diffusivity is determined from the transient temperature response of the sample. The thermal diffusivity, α, was calculated using the half-rise time method:

$$\alpha = 0.1388 \frac{d^2}{t_{\frac{1}{2}}} \tag{2.1}$$

where d is the sample thickness and $t_{\frac{1}{2}}$ is the time required for the rear surface temperature to reach one half of its maximum value. The thermal conductivity, k, was then calculated from the measured thermal diffusivity using:

$$k = \alpha \rho C_p \tag{2.2}$$

where ρ is the density and C_p is the specific heat of the corresponding composite sample. This approach allowed the thermal conductivity of pure epoxy and epoxy/graphene composites prepared using acetone and DMF to be compared as a function of graphene loading.

Laser scanning confocal microscopy (LSCM) was used to characterize the dispersion of graphene nanoplatelets within the cured epoxy matrix. Confocal microscopy provides optical sectioning by rejecting out-of-focus light using a spatial pinhole, which improves image contrast compared with conventional optical microscopy[51-53]. This technique was selected because it enables visualization of graphene-rich regions and graphene-poor regions within the composite, making it useful for comparing the relative dispersion quality obtained using acetone and DMF. Confocal microscopy images were collected for epoxy/graphene composites prepared at 3wt%, 5wt%, and 7wt% graphene loading for both solvent systems.

The confocal microscopy images were further analyzed using Fiji/ImageJ software to quantify graphene agglomeration. The image analysis was used to estimate the maximum agglomerate volume in each sample. This quantitative analysis provided a way to compare the extent of graphene agglomeration in acetone- and DMF-processed composites beyond visual

inspection of the microscopy images. The maximum agglomerate volume was used as a representative measure of the largest graphene-rich regions formed during composite processing.

Graphene suspension stability in acetone and DMF was also evaluated visually as a supporting comparison of solvent-assisted dispersion behavior. Graphene suspensions were observed at different times after dispersion, including 0 h, 5 h, and 24 h. These observations were used to compare the tendency of graphene nanoplatelets to remain suspended or settle in each solvent. The suspension stability results were used as supporting evidence for the dispersion behavior observed in the cured composites.

Effective medium theory was used to interpret the measured thermal conductivity values in terms of an apparent thermal interface resistance between graphene nanoplatelets and the epoxy matrix. In this analysis, graphene nanoplatelets were treated as oblate filler particles dispersed within an epoxy matrix. A random filler orientation was assumed, corresponding to an orientation factor of 1/3. The model accounts for the effect of thermal interface resistance by using effective in-plane and through-plane thermal conductivity values for the graphene filler rather than only the intrinsic graphene thermal conductivity. The apparent interface resistance was then adjusted to fit the experimentally measured thermal conductivity values for acetone- and DMF-processed composites. The interface resistance obtained from this approach should be interpreted as an effective transport parameter because it includes not only the local graphene-epoxy interface resistance, but also the effects of filler dispersion, agglomeration, and assumptions in the effective medium model.

2.3 Results and Discussion

The thermal conductivity of epoxy/graphene composites prepared using acetone and DMF is shown in Figure 2.2 as a function of graphene loading. The thermal conductivity of the pure epoxy sample was measured to be 0.17 $Wm^{-1}K^{-1}$. Incorporation of graphene nanoplatelets increased the thermal conductivity of the epoxy matrix for both solvent systems, confirming the role of graphene as an effective thermally conductive filler. At 3wt% graphene loading, both acetone- and DMF-processed composites showed the same thermal conductivity value of 0.34 $Wm^{-1}K^{-1}$. This indicates that, at low graphene loading, the influence of solvent selection on thermal conductivity is limited. At this concentration, the graphene nanoplatelets are more separated from one another, and the probability of forming large agglomerates is relatively low. Therefore, both solvents are able to disperse the graphene sufficiently to produce similar thermal transport behavior.

At higher graphene loadings, however, the effect of solvent selection became more significant. At 5wt% and 7wt% graphene loading, the composites prepared using DMF showed higher thermal conductivity than those prepared using acetone. The difference was most pronounced at 7wt%, where the DMF-processed composite showed 44% higher thermal conductivity than the acetone-processed composite. This result demonstrates that solvent selection becomes increasingly important as graphene concentration increases. At higher filler loading, graphene-graphene interactions become stronger and the tendency for reaggregation increases. Under these conditions, the ability of the solvent to stabilize the graphene dispersion before curing becomes more important for determining the final composite microstructure and thermal conductivity.

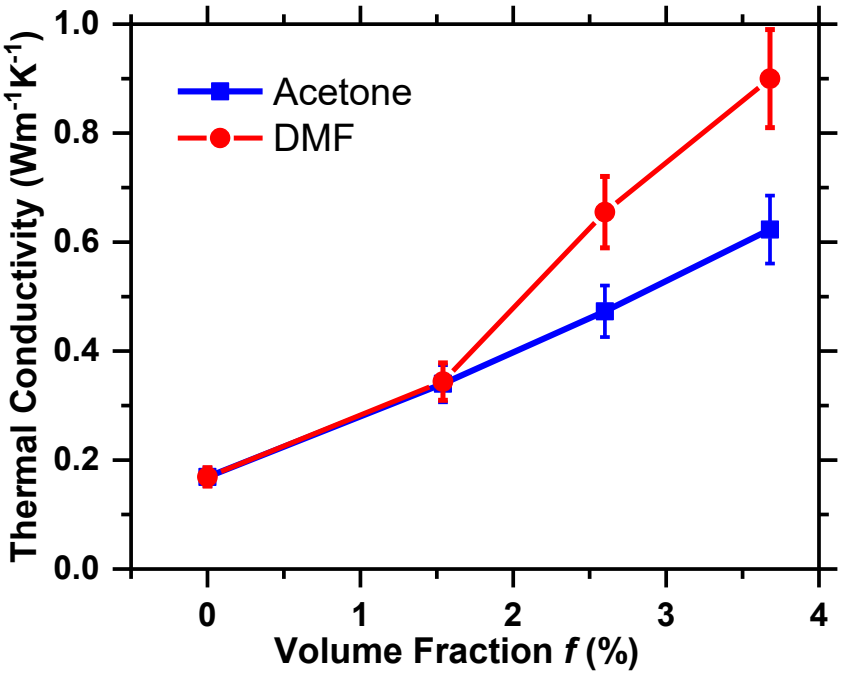


Figure 2.2 Thermal conductivity of graphene/epoxy composites prepared using two different solvents with increasing graphene concentration

The difference in thermal conductivity between acetone- and DMF-processed composites can be explained by differences in graphene dispersion within the cured epoxy matrix. Laser scanning confocal microscopy images of the composite samples are shown in Figure 2.3. In the figure, black regions correspond to epoxy and red spots correspond to the graphene nanoplatelets. Acetone-processed samples showed larger graphene agglomerations and larger epoxy regions between the agglomerates, indicating less uniform graphene dispersion. In contrast, the DMF-processed samples showed a more homogeneous distribution of graphene nanoplatelets throughout the epoxy matrix. This difference in dispersion was especially noticeable at higher graphene loadings, where agglomeration becomes more likely. The confocal microscopy results therefore support the thermal conductivity measurements by showing that the higher thermal conductivity of DMF-processed composites is associated with improved graphene distribution.

The confocal microscopy images were further analyzed using Fiji/ImageJ to estimate the maximum graphene agglomerate volume in each composite. The maximum agglomerate volume comparison is shown in Figure 2.5a. At 3wt% graphene loading, the agglomerate sizes in acetone- and DMF-processed composites were similar, which is consistent with the identical thermal conductivity values measured at this loading. At 5wt% and 7wt%, however, the acetone-processed samples contained significantly larger agglomerates. The maximum agglomerate volume in the acetone-processed composite was 211% higher than that of the DMF-processed composite at 5wt% and 93% higher at 7wt%. These results quantitatively confirm that DMF reduces graphene agglomeration relative to acetone during composite processing.

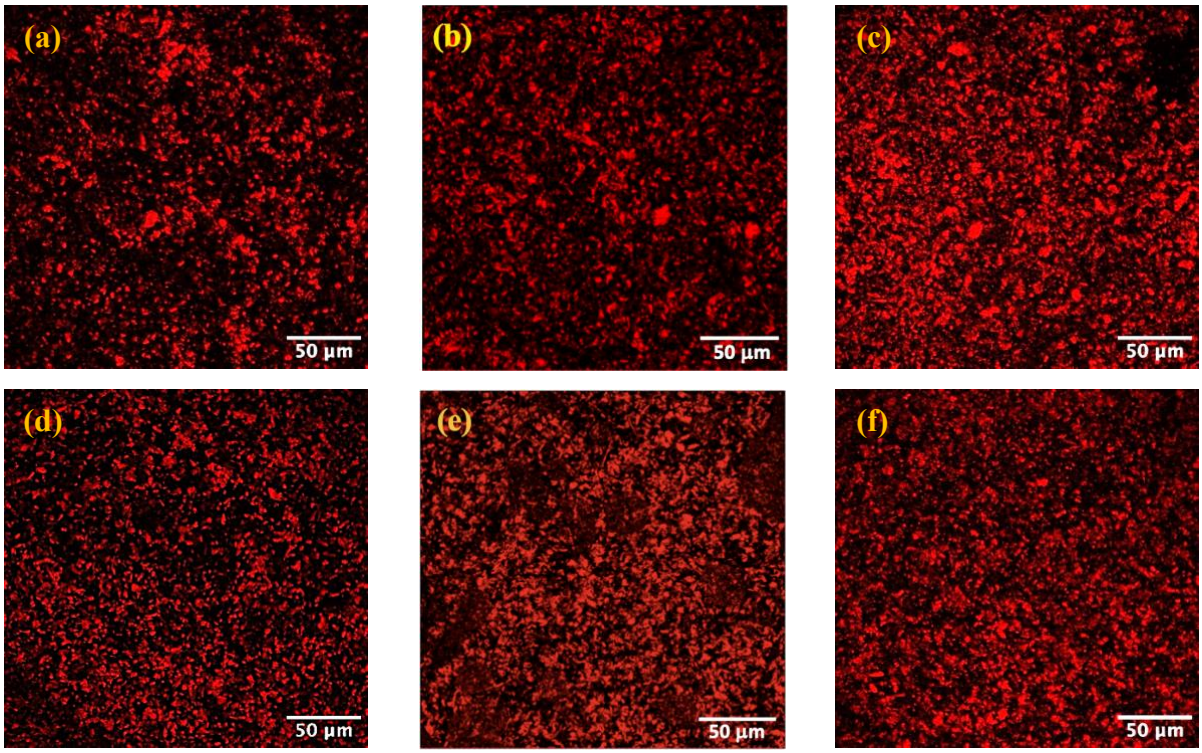


Figure 2.3 Confocal microscopy images for acetone-based samples for concentrations a) 3wt%, b) 5wt%, c) 7wt% and DMF-based samples for concentrations d) 3wt%, e) 5wt%, f) 7wt%

The relationship between agglomeration and thermal conductivity can be understood by considering the role of graphene distribution in heat transfer. Graphene-rich agglomerates may contain locally high filler concentration, but they do not necessarily produce efficient heat transport across the entire composite. Large agglomerates reduce the effective contact area between graphene and epoxy and create nonuniform regions within the composite. In graphene-poor regions, heat must travel primarily through the low-thermal-conductivity epoxy matrix. In graphene-rich agglomerated regions, the filler may be poorly connected to the surrounding matrix, limiting the ability of heat to enter and leave the agglomerate efficiently. As a result, large agglomerates can reduce the effectiveness of graphene as a thermal transport pathway. A more uniform filler distribution, as observed in the DMF-processed samples, increases the probability of forming distributed thermal pathways and improves effective graphene-epoxy contact.

The graphene suspension stability comparison shown in Figure 2.4 provides additional support for the improved dispersion behavior of DMF. Graphene suspensions in acetone and DMF were observed at different times after dispersion. The DMF suspension showed better stability over time, while the acetone suspension showed a greater tendency toward settling and reaggregation. This observation is consistent with the reported dispersion behavior of graphene in DMF and supports the confocal microscopy results obtained from the cured composites. Although suspension stability alone does not fully determine the final composite morphology, it provides useful evidence that DMF is more effective than acetone in maintaining graphene dispersion during the early stages of processing.

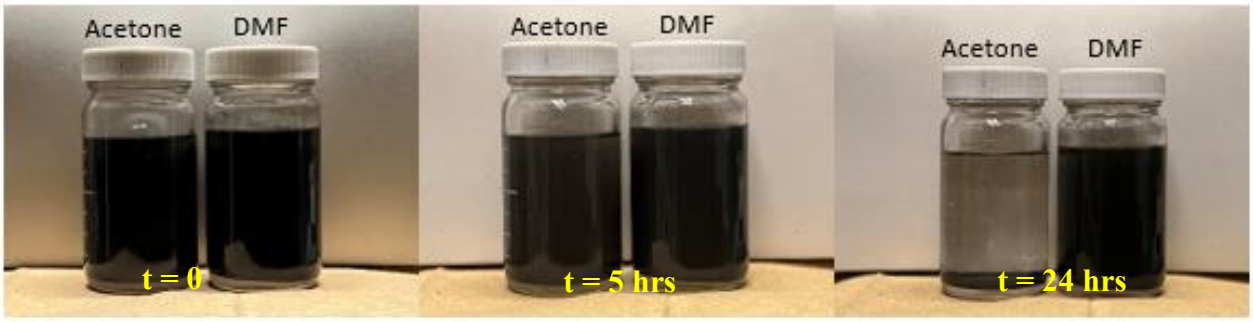


Figure 2.4 Graphene suspension in acetone and DMF at t = 0, 5 and 24 hours

Effective medium theory was used to further interpret the measured thermal conductivity values in terms of apparent thermal interface resistance. This was done using the theory presented by Nan *et al*[19]. From this theory, the theoretical effective thermal conductivity of epoxy/gnp composites is given by

$$k_{effective} = k_m \frac{2 + f[\beta_{11}(1 - L_{11})(1 + \langle \cos^2 \theta \rangle + \beta_{33}(1 - L_{33})(1 - \langle \cos^2 \theta \rangle)]}{2 + f[\beta_{11} L_{11}(1 + \langle \cos^2 \theta \rangle) + \beta_{33} L_{33}(1 - \langle \cos^2 \theta \rangle)]} \tag{2.3}$$

where $k_{effective}$ and k_m are the effective thermal conductivities of composite and pristine epoxy matrix respectively, for f volume fraction of graphene nanoparticles. The $\langle \cos^2 \theta \rangle$ term considers the orientation of the filler material. For the present scenario, a random orientation of graphene nanoparticles is considered ($\langle \cos^2 \theta \rangle$=1/3).

The geometrical parameters of the oblate graphene nanoparticles such as L_{ii} are obtained by using the following equations (p is the aspect ratio):

$$L_{11} = L_{22} = \frac{p^2}{2(p^2 - 1)} + \frac{p}{2(1 - p^2)^{3/2}} \cos^{-1} p \tag{2.4}$$

$$L_{33} = 1 - 2L_{11}$$

In equation 2.3, the term β_{ii} is a function of the thermal interface resistance and is computed using the equation:

$$\beta_{ii} = \frac{K_{ii}^c - k_m}{k_m + L_{ii}(K_{ii}^c - k_m)} \tag{2.5}$$

where K_{ii}^c are the effective thermal conductivity values of the graphene nanoparticles considering the effect of thermal interface resistance. The in-plane effective values K_{11}^c, K_{22}^c and the through-plane effective value K_{33}^c are given by equations:

$$K_{11}^c = K_{22}^c = \frac{k_{pi}}{1 + \gamma L_{11}\, k_{pi}/k_m} \tag{2.6}$$

$$K_{33}^c = \frac{k_{pt}}{1 + \gamma L_{33}\, k_{pt}/k_m} \tag{2.7}$$

$$\gamma = (1 + 2p)\alpha \tag{2.8}$$

$$\alpha = \frac{R k_m}{t} \tag{2.9}$$

where R is the thermal interface resistance and k_{pi} and k_{pt} are the in-plane and through-plane thermal conductivities of graphene, respectively.

The interface thermal resistance values calculated from this theory are shown in figure 2.5b along with a comparison between the measured thermal conductivity values and EMT predictions. The fitted apparent interface resistance for the acetone-processed composites was higher than that for the DMF-processed composites. Specifically, the EMT fitting gave an apparent interface resistance of 5.64 x 10^{-8} m^2KW^{-1} for the acetone-processed composites and 3.1 x 10^{-8} m^2KW^{-1} for the DMF-processed composites. The lower apparent interface resistance for the DMF-based composites is consistent with improved graphene dispersion and better effective contact between graphene nanoplatelets and epoxy.

The interface resistance obtained from EMT should be interpreted carefully. It does not represent only the intrinsic resistance of a single ideal graphene-epoxy interface. Instead, it is an effective or apparent parameter that captures several microstructural effects, including filler dispersion, agglomeration, graphene-epoxy contact area, and assumptions in the effective medium model. Therefore, the lower fitted interface resistance for the DMF-processed composites indicates that the overall heat-transfer environment in these composites is more favorable. Improved dispersion reduces large agglomerates and increases the effective filler-polymer contact area, allowing heat to move more efficiently between the epoxy matrix and graphene nanoplatelets.

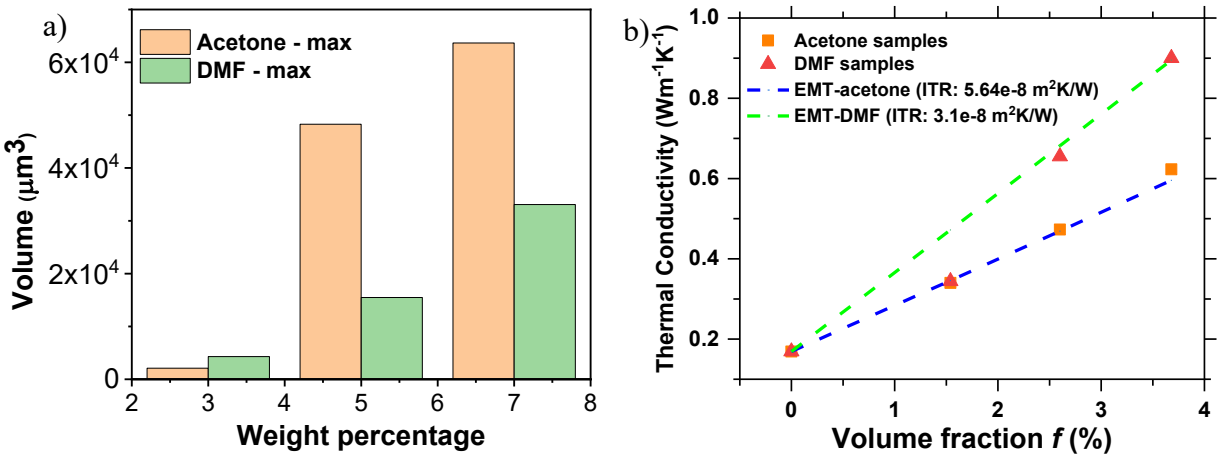


Figure 2.5 a) Maximum graphene agglomeration volume comparison, b) Effective medium theory and measured thermal conductivity values.

2.4 Conclusions

This chapter investigated the effect of solvent selection on the dispersion of graphene nanoplatelets and the resulting thermal conductivity of epoxy/graphene composites. Acetone and DMF were compared as processing solvents for composites containing 3wt%, 5wt%, and 7wt% graphene nanoplatelets. The purpose of this comparison was to determine whether improved

solvent-assisted dispersion could reduce graphene agglomeration and improve thermal transport in the epoxy matrix.

The thermal conductivity results showed that both acetone- and DMF-processed composites enhanced the thermal conductivity of epoxy after graphene addition. At 3wt% graphene loading, both solvent systems produced similar thermal conductivity, indicating that solvent effects were limited at low filler loading. However, at higher graphene loadings, the DMF-processed composites showed higher thermal conductivity than the acetone-processed composites. This result demonstrates that solvent selection becomes more important as graphene loading increases and the tendency for graphene reaggregation becomes stronger.

Confocal microscopy showed that the DMF-processed composites contained a more uniform distribution of graphene nanoplatelets, while acetone-processed composites showed larger graphene-rich agglomerates and less uniform dispersion. Quantitative image analysis confirmed that acetone-based composites contained larger maximum agglomerate volumes at higher graphene loadings. These results indicate that DMF is more effective than acetone in maintaining graphene dispersion during composite processing. The improved dispersion increases the effective contact between graphene nanoplatelets and epoxy and supports more efficient heat transfer through the composite.

Effective medium theory further supported this interpretation by showing lower apparent thermal interface resistance for the DMF-processed composites compared with the acetone-processed composites. This apparent interface resistance should be understood as an effective transport parameter that includes the combined effects of graphene-epoxy interface resistance, filler dispersion, agglomeration, and model assumptions. The lower apparent resistance for DMF-

based composites is consistent with improved filler distribution and more effective graphene-epoxy contact.

Overall, this chapter demonstrates that solvent-assisted dispersion is an important processing strategy for improving the thermal conductivity of epoxy/graphene composites. DMF improved graphene dispersion relative to acetone, reduced agglomeration, lowered the apparent thermal interface resistance, and produced higher thermal conductivity at higher graphene loadings. These findings address the first major challenge of this dissertation: graphene nanoplatelet agglomeration in epoxy composites. While improved dispersion enhances the effectiveness of graphene nanoplatelets, the composite still contains discrete graphitic fillers with many filler-filler contacts. Therefore, the next chapter investigates expanded graphite as a strategy to improve graphitic filler connectivity and further enhance thermal transport in epoxy-based composites.

Chapter 3

Enhancement of Epoxy Composites Thermal Conductivity Using Expanded Graphite

3.1 Introduction and Background

3.1.1 Introduction

As discussed in Chapter 1, the thermal conductivity of epoxy/graphene-based composites is governed not only by the intrinsic thermal conductivity of the graphitic filler, but also by the internal filler structure formed inside the polymer matrix. Graphene-based fillers possess high in-plane thermal conductivity and are therefore attractive for improving heat conduction in epoxy composites[1,3,54,55]. However, the effective thermal conductivity of the final composite depends strongly on filler dispersion, filler-filler connectivity, polymer-filler interfaces, and the degree to which the graphitic filler network provides continuous pathways for heat transport. Chapter 2 addressed the role of solvent-assisted dispersion in reducing graphene agglomeration in epoxy composites. The present chapter focuses on a different limitation: the dependence of heat transport on repeated contacts between discrete graphitic particles.

In epoxy composites containing discrete graphene nanoplatelets, heat must pass through the polymer matrix, through individual graphitic fillers, and across numerous filler-filler junctions. Although graphene nanoplatelets have high intrinsic in-plane thermal conductivity, the full benefit of this property is difficult to achieve when the thermally conductive network is interrupted by polymer-rich regions or by many discrete particle-particle contacts. These contacts can introduce

thermal contact limitations, especially when the fillers are not well connected or when the contact area between neighboring particles is small[29,56]. Therefore, improving thermal conductivity requires not only the addition of a high-conductivity filler, but also the formation of a more efficient graphitic network within the epoxy matrix.

Table 3.1 Thermal Conductivities of epoxy/EG composites

Filler	Filler Concentration	$k_{composite}$ ($W \cdot m^{-1} \cdot K^{-1}$)	*k* Increase (%)	Reference
EG-BN	5-70wt%	2.22	1010	Isarn *et al.*[57]
Ag plated EG-G-Cu	10phr = 10wt%	1.71	755	Yim *et al.*[58]
EG-G-Cu	10phr	1.36	580	Yim *et al.*[58]
KH550@EG	4.5wt%	1	400	Wang *et al.*[59]
EG	40wt%	3.36	1876	Jin *et al.*[60]

Expanded graphite provides a promising strategy to improve graphitic network connectivity. Expanded graphite is typically prepared by chemically intercalating graphite to form graphite intercalated compounds, followed by rapid thermal expansion at high temperature. During expansion, intercalated species generate pressure between graphite layers, causing the graphite to expand into a porous, worm-like structure. Unlike isolated graphene nanoplatelets, expanded graphite can preserve partially connected, worm-like graphitic structure that provides longer continuous pathways for heat transport within the epoxy matrix. When incorporated into epoxy, this expanded structure may help form more continuous graphitic pathways and reduce the extent to which heat transport depends on many isolated filler-filler junctions. This does not mean that expanded graphite eliminates polymer-filler interface resistance or filler-filler contact resistance. Rather, the expected advantage is that expanded graphite can reduce the severity of repeated discrete contact limitations by providing a more connected graphitic architecture[13,15,31,61-64].

Several studies have demonstrated the effectiveness of expanded graphite as a thermally conductive filler in polymer composites. Expanded graphite networks have been used to increase thermal conductivity in matrix systems such as linear low-density polyethylene, polydimethylsiloxane, phase change materials, polyetherimide, and epoxy. In these systems, the enhancement in thermal conductivity is commonly attributed to the formation of continuous or semi-continuous graphitic pathways through the polymer matrix[13,14,31,60,62,63].

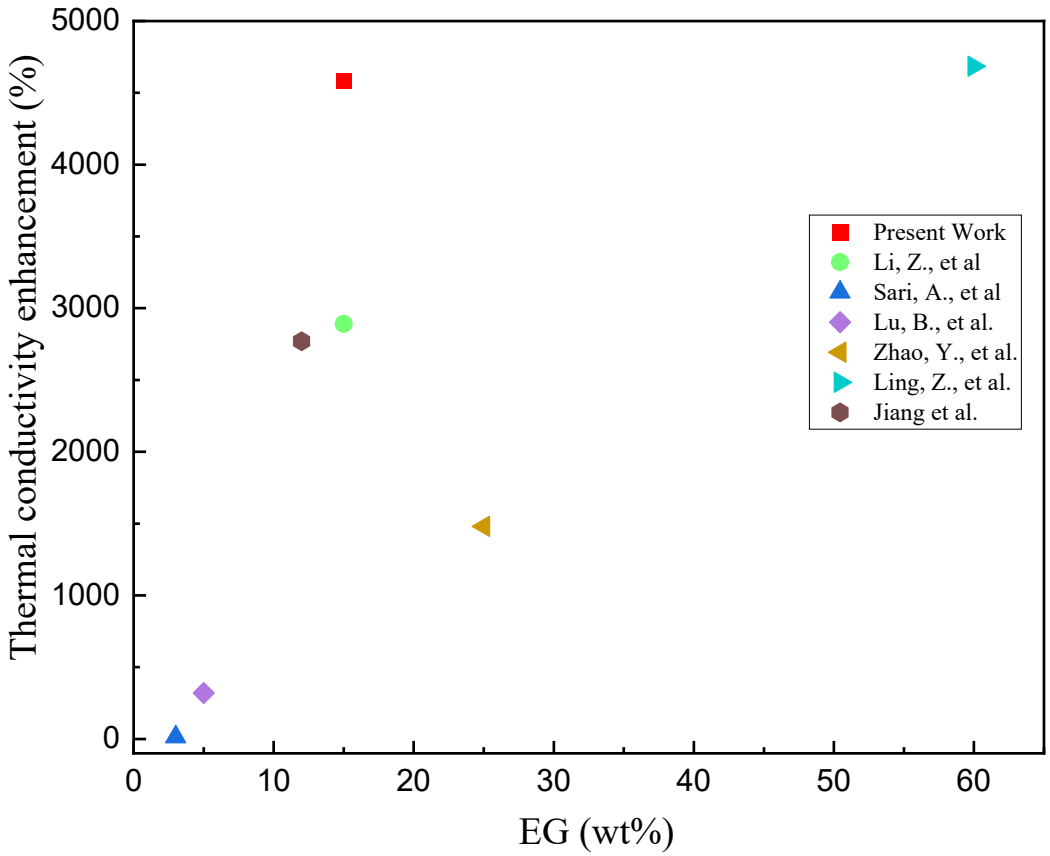


Figure 3.1 Enhancement in thermal conductivity for different EG/Epoxy composites

Despite these advantages, the properties of expanded graphite depend strongly on the graphite intercalation process used to produce it. Many studies use commercially available expanded graphite or graphite intercalated compounds, where the details of the intercalation chemistry are not always known. However, the final morphology, expansion behavior, defect density, and chemical composition of expanded graphite are affected by the type and amount of acid, oxidizing agent, reaction time, and thermal expansion conditions[65-68]. These factors can influence the ability of expanded graphite to form connected pathways in epoxy and can also affect the intrinsic quality of the graphitic structure. Therefore, optimizing the intercalation reaction is important for developing epoxy/expanded graphite composites with improved thermal transport.

Graphite consists of stacked graphene layers held together by relatively weak van der Waals forces, with an interlayer spacing of approximately 3.35 Å[69,70]. Chemical intercalation introduces atoms, ions, or molecules between these graphitic layers, forming graphite intercalated compounds (GICs). More details on GIC are given in the following section. In acid-based intercalation routes, sulfuric acid is commonly used as the acidic medium, while an oxidizing agent assists the intercalation process by weakening the interaction between graphite layers and enabling insertion of intercalated species. The resulting graphite intercalated compounds can expand rapidly when exposed to high temperature, producing expanded graphite with increased volume and porous graphitic morphology[71].

In this chapter, hydrogen peroxide and sulfuric acid are used to prepare graphite intercalated compounds for subsequent thermal expansion. In the H_2O_2/H_2SO_4 route, H_2SO_4 provides the acidic intercalation environment, while H_2O_2 acts as the oxidizing agent. The H_2O_2-based reaction can produce noticeable pre-expansion of graphite during the intercalation step,

which has been associated with decomposition of H_2O_2 and gas evolution within or near the graphite galleries[30]. This pre-expansion behavior can increase the volume of the graphite intercalated compound before the high-temperature expansion step. However, the reaction must be controlled carefully because excessive reaction severity may damage the graphitic structure, increase defect density, or fragment the expanded graphite, all of which can limit the thermal conductivity of the final composite.

The objective of this chapter is to investigate epoxy/expanded graphite composites prepared using the H_2O_2/H_2SO_4 graphite intercalation route. Short-duration H_2O_2/H_2SO_4 reactions are used to prepare graphite intercalated compounds, which are then thermally expanded to obtain H_2O_2-derived expanded graphite. These fillers are incorporated into epoxy, and the resulting composites are evaluated through thermal diffusivity, thermal conductivity, and Raman spectroscopy. The reaction conditions are optimized based on the thermal transport performance of the epoxy/H_2O_2-EG composites.

The working hypothesis of this chapter is that optimized H_2O_2-derived expanded graphite can improve epoxy thermal conductivity by forming more connected graphitic pathways within the polymer matrix. The interpretation is intentionally cautious: the improvement is attributed to enhanced graphitic network connectivity, rather than complete removal of polymer-filler or filler-filler thermal resistance. Remaining limitations may still arise from polymer-filler interfacial resistance, structural defects introduced during intercalation, filler fragmentation during processing and void formations in the prepared composite samples. By focusing on the H_2O_2/H_2SO_4 route, this chapter evaluates how graphite intercalation and thermal expansion can be used to improve filler connectivity in epoxy-based thermal management composites.

3.1.2 Graphite Intercalated Compounds

Graphite intercalated compounds (GICs), as shown in figure 3.2, are formed when chemical species are inserted between the stacked graphene layers of graphite. Depending on the direction of charge transfer between the graphite lattice and the intercalated species, GICs are commonly classified as either acceptor-type or donor-type compounds. In an acceptor-type GIC, an electronegative intercalating species accepts electrons from the π-electron network of graphite, resulting in a positively charged graphite host and negatively charged intercalated species. This process can be represented as:

$$C_x + A \rightleftharpoons C_x^{m+}.A^{m-} \tag{3.1}$$

where C_x represents the graphite structure and A represents the acceptor species. In contrast, donor-type GICs form when the intercalated species donates electrons to the π-electron network of graphite[72,73]. These are commonly associated with metallic intercalants and can be represented as:

$$C_x + A \rightleftharpoons C_x^{m-}.A^{m+} \tag{3.2}$$

During intercalation, the starting graphite can undergo simultaneous oxidation or reduction depending on the nature of the intercalating species. The charge transfer associated with acceptor- or donor-type intercalation generates electrostatic repulsion between adjacent graphite layers. This repulsion increases the relative interlayer spacing and assists further penetration of intercalating species into the graphite galleries[74]. As a result, intercalation weakens the interaction between the stacked graphene layers, thus creating a graphitic structure than can expand during subsequent thermal treatment.

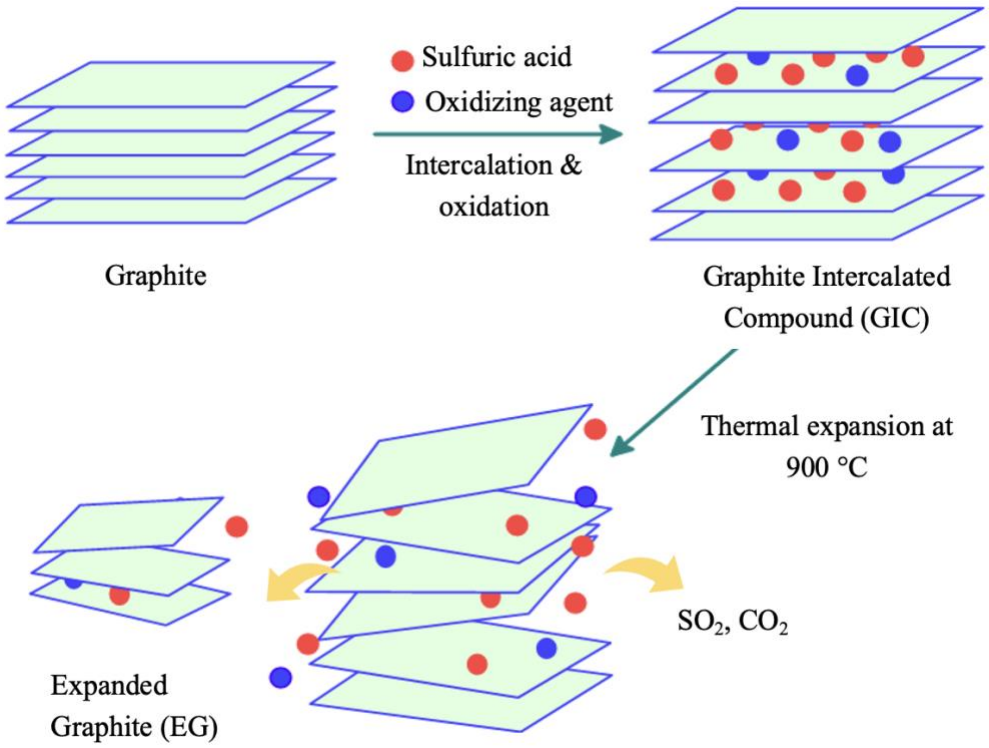


Figure 3.2 Diagram depicting the preparation process of graphite intercalation compounds (GIC) using acids and oxidizing agents, followed by thermal expansion to produce expanded graphite (EG)

When sulfuric acid is used with an oxidizing agent, a specific class of GICs known as graphite bisulfates can be formed. In these compounds, graphite layers are intercalated by bisulfate ions ($HSO4^-$) and sulfuric acid molecules (H_2SO_4). The formation kinetics and intercalation stage of graphite bisulfates depend on the sulfuric acid concentration, the type of oxidizing agent, the oxidizing agent concentration, and the reaction time[75]. The general formation of graphite bisulfates can be described by the following reaction scheme[30,76]:

$$24nC + O_x^z + mH_2SO_4 \rightarrow C_{24_n}^+ \cdot HSO4^- \times (m-1)H_2SO_4 + HO_x^{(z-1)} \qquad (3.3)$$

where O_x represents the oxidizing agent, C represents carbon atoms in the graphite structure, and m and n represent the number of moles of carbon and sulfuric acid, respectively. In this reaction,

the primary function of the acid is to provide the intercalation species (like bisulfate ions coming from H_2SO_4) and the oxidizing agent weakens the bonding between the graphite layers, thus promoting anionic and molecular insertion into the interlayer spacing of graphite through its redox activity. The resulting GICs contain carbon, oxygen, and sulfur species in different proportions depending on the intercalation chemistry.

The presence of intercalated species and oxygen-containing groups gives GICs the ability to expand upon rapid thermal heating. During thermal expansion, intercalated species decompose, volatilize, or generate internal pressure between graphite layers, forcing the stacked layers apart and producing expanded graphite. Therefore, GICs serve as important precursors for preparing expanded graphite fillers. However, the final expanded graphite structure is strongly dependent on the GIC synthesis conditions[77-79]. Parameters such as acid concentration, oxidizing agent type, oxidizing agent amount, and reaction time can influence the degree of intercalation, extent of expansion, defect formation, and preservation of the graphitic structure.

In this work, graphite intercalation was used as the precursor step for preparing expanded graphite fillers for epoxy composites. The intercalation reaction was optimized by varying oxidizing agent chemistry and reaction conditions, with particular attention to the relationship between GIC formation, subsequent thermal expansion, and composite thermal conductivity. Hydrogen peroxide (H_2O_2) was investigated as an oxidizing agent in the broader reaction optimization study, while sulfuric acid was used as the common acidic intercalation medium. The optimization focused on two main reaction parameters: oxidizing agent concentration and reaction time. Short reaction times were explored to identify a faster and more efficient route for producing expanded graphite capable of improving epoxy composite thermal conductivity. The results from

this optimization showed that the choice of oxidizing agent and reaction condition strongly influenced the thermal transport performance of the resulting epoxy/expanded graphite composites.

3.2 Materials and Experimental Methods

3.2.1 Materials

Natural flake graphite (−10 mesh, 99.9%) was purchased from Alfa Aesar, USA, and used as the starting graphite precursor for the intercalation reaction. Sulfuric acid (H_2SO_4, ACS reagent, 95–98%, product no. 258104, Sigma-Aldrich) was used as the primary intercalating agent. Hydrogen peroxide solution (H_2O_2, 30wt% in H_2O, contains inhibitor, ACS reagent, product no. 216763-100mL, Sigma-Aldrich) was used as the oxidizing agent in the H_2O_2/H_2SO_4 intercalation mixture. The epoxy resin and curing agent used for composite fabrication were EPIKOTE RESIN MGS RIMR 135 and EPIKURE CURING AGENT MGS RIMH 137, respectively, both obtained from Hexion.

3.2.2 H_2O_2/H_2SO_4 Intercalation Process and Synthesis of EG

The H_2O_2/H_2SO_4 intercalation route was used to prepare graphite intercalated compounds (GICs) from natural flake graphite. In this process, sulfuric acid served as the intercalating acid medium, while hydrogen peroxide was used as the oxidizing agent. The intercalation reaction was optimized by varying the reaction time while maintaining a constant volumetric ratio of H_2SO_4 to H_2O_2. For all H_2O_2-based reactions, the H_2SO_4:H_2O_2 volume ratio was kept at 4:1. Two acid/oxidant combinations were used: 24 mL H_2SO_4 with 6 mL H_2O_2 and 20 mL H_2SO_4 with 5 mL

H_2O_2. The reaction times were varied between 3 and 7 min to evaluate the effect of intercalation duration on the resulting expanded graphite and its composite thermal transport performance. The H_2O_2/H_2SO_4 reaction conditions used in this study are summarized in Table 3.1. For the 24 mL H_2SO_4/6 mL H_2O_2 condition, reaction times of 3, 4, 5, 6, and 7 min were studied. For the 20 mL H_2SO_4/5 mL H_2O_2 condition, reaction times of 3, 5, and 7 min were studied. These reaction conditions were selected after initial trial reactions and were used to identify the intercalation condition that produced the best thermal transport performance in epoxy/expanded graphite composites.

The intercalation reactions were conducted at room temperature. In a typical reaction, the required volume of sulfuric acid was first added to a flask. Then, 2 g of −10 mesh graphite flakes were added to the acid and stirred for 5 min at 150 rpm using a magnetic stirrer. After this initial graphite/acid mixing step, the required volume of H_2O_2 was slowly added to the flask. The reaction was then allowed to proceed for the selected reaction time listed in Table 3.2. During the H_2O_2/H_2SO_4 intercalation process, visible pre-expansion of the graphite flakes was observed. This pre-expansion resulted in the formation of high-volume graphite intercalated compounds and, in some reactions, was large enough to hinder the stirring motion inside the flask. This observation indicates that the H_2O_2/H_2SO_4 route produced significant expansion of the graphite structure even before the high-temperature thermal expansion step. The extent of this pre-expansion was considered an important processing feature of the H_2O_2-based intercalation route.

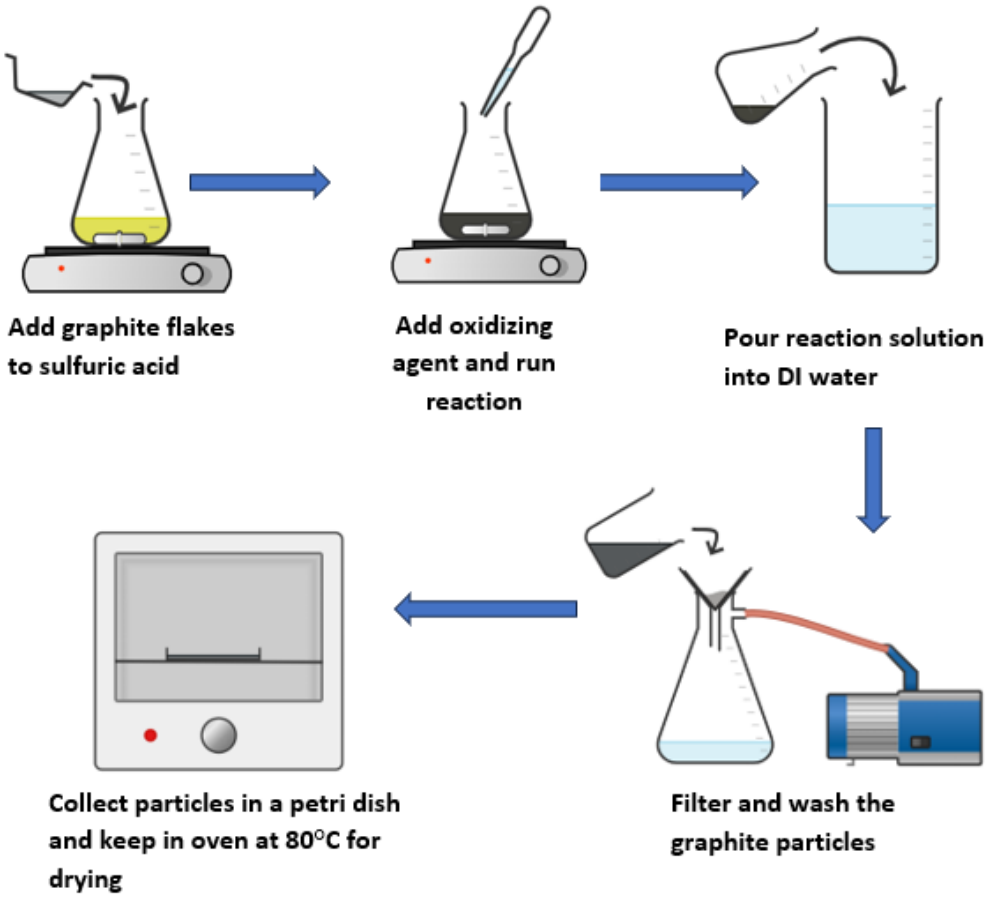


Figure 3.3 Schematic for graphite intercalation procedure

After completion of the reaction, the reaction mixture was transferred into a beaker containing 400 mL deionized water. The resulting product was filtered and washed sequentially with deionized water, ethanol, and acetone. After washing, the graphite particles were transferred to a petri dish and dried in a convection oven at 80 °C. The dried product obtained after this process is referred to as H_2O_2-GIC.

Table 3.2 H_2O_2/H_2SO_4 intercalation reaction conditions

Sample Name (GIC & EG)	-10 Mesh Graphite (g)	H_2SO_4 (mL)	H_2O_2 (mL)	Volume Ratio (H_2SO_4: H_2O_2)	Time (min)
SD-H1	2	24	6	4:1	3
SD-H2	2	24	6	4:1	4
SD-H3	2	24	6	4:1	5
SD-H4	2	24	6	4:1	6
SD-H5	2	24	6	4:1	7
SD-H6	2	20	5	4:1	3
SD-H7	2	20	5	4:1	5
SD-H8	2	20	5	4:1	7

The H_2O_2-GIC was then thermally expanded in a muffle furnace pre-heated to ~940°C. A ceramic crucible filled with small amounts of GICs was placed in the furnace for 35-40 seconds to allow the GICs to expand to form the EG, following which the crucible was taken out and allowed to cool to room temperature. This GIC expansion was conducted under ambient air atmosphere, without any inert or controlled gas environment.

3.2.3 Preparation of Epoxy/Expanded Graphite Composite Samples

Epoxy/expanded graphite (epoxy/EG) composite samples were prepared using the expanded graphite obtained from the thermally expanded graphite intercalated compounds described in Section 3.2.2. For each composite formulation, the required epoxy resin mass was calculated based on the target EG loading. The epoxy resin was first added to 200 mL of acetone and mixed to form an epoxy/acetone solution prior to filler addition. This solution was then tip-sonicated at room temperature for 20 min at 20% amplitude using pulse mode, with 3 seconds on and 1 second off, to promote uniform mixing of the resin in the solvent.

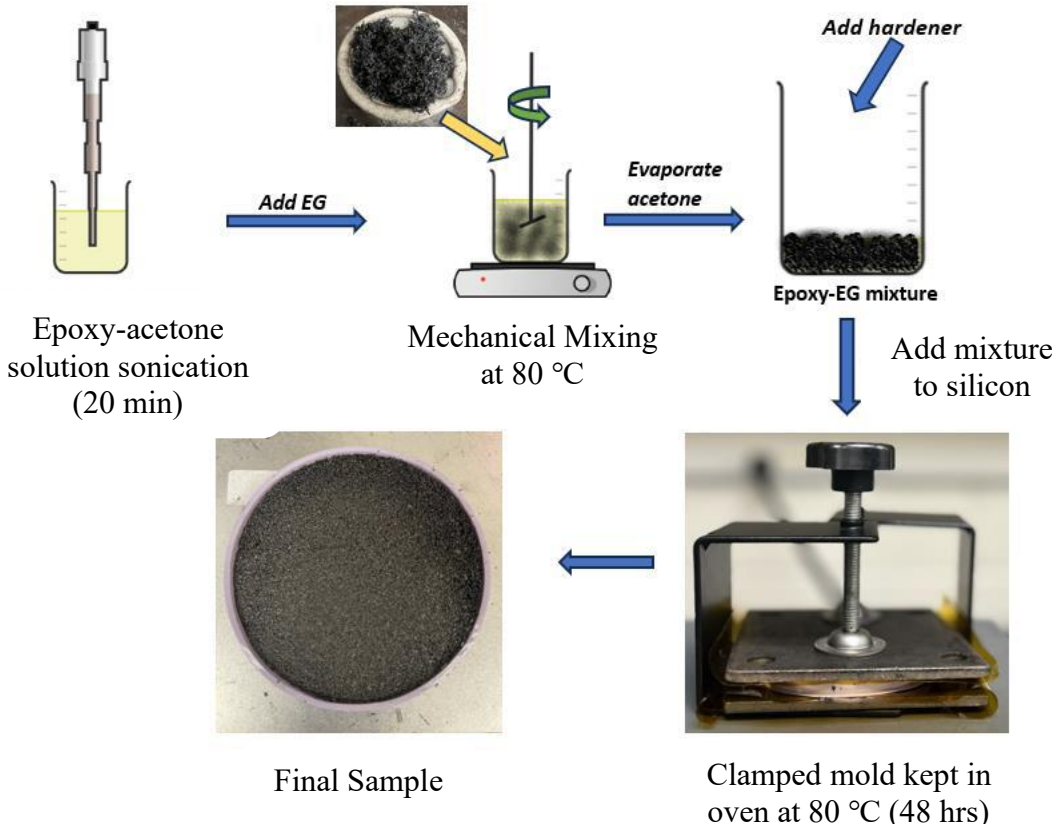


Figure 3.4 Schematic illustration for preparation technique of epoxy/EG composite

After sonication, the required amount of expanded graphite was added to the epoxy/acetone solution. The mixture was then mechanically mixed at 70 °C until the acetone fully evaporated, resulting in a dry epoxy/EG mixture. The heating and mixing step was used to remove the solvent while allowing the expanded graphite to be incorporated into the epoxy resin. After solvent removal, the curing agent, EPIKURE CURING AGENT MGS RIMH 137, was added at 30wt% relative to the epoxy resin mass, corresponding to a resin: hardener mass ratio of 100:30. The mixture was manually mixed using a wooden stir stick for approximately 1–2 min until it appeared visually uniform and spreadable.

The prepared epoxy/EG mixture was then transferred to a silicone mold. The mold was clamped to maintain closure and promote consistent specimen thickness during curing. The samples were cured in a convection oven at 80 °C for 48 h. After curing, the mold was removed from the oven and allowed to cool to room temperature. Circular samples with a diameter of 0.5 in. were then punched from the cured composite sheet for thermal characterization.

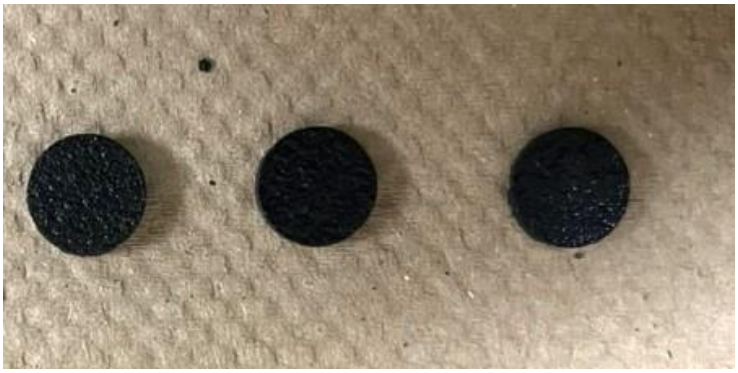


Figure 3.5 Optical images of half-inch circular Epoxy-EG samples prepared for thermal diffusivity measurements

Before thermal diffusivity measurements, the punched samples were coated with graphite to improve absorption of the laser pulse and infrared detection during laser flash analysis. The overall epoxy/EG composite fabrication procedure is illustrated in Figure 3.4 and representative punched samples used for thermal diffusivity testing are shown in Figure 3.5. All the three samples shown are from a single weight percentage sample. Thermal diffusivity measurement, thermal conductivity calculation, and density determination are described in Section 3.2.4.

3.2.4 Measurements and Characterization

Through-thickness thermal diffusivity (α) of the epoxy/EG composite samples was measured using a laser flash apparatus (NETZSCH LFA 467 HyperFlash) at 25 °C. Circular

specimens with a diameter of 12.7 mm and thickness in the range of 2–4 mm were used for the measurements. Prior to testing, both faces of each specimen were coated with DGF 123 dry graphite film spray and air-dried for 1–2 min to improve laser absorption and infrared detection. For each specimen, thermal diffusivity was obtained by averaging three consecutive flashes. The diffusivity data were analyzed using the Cowan model implemented in the instrument software. Thermal conductivity (k) was calculated using:

$$k = \alpha \rho C_p \tag{3.4}$$

where α is the measured thermal diffusivity, ρ is the density, and C_p is the specific heat capacity of the sample. Density was measured by helium gas pycnometry using an AccuPyc II 1340 pycnometer (Micromeritics). Specific heat capacity was obtained using the rule of mixtures. A total of 8–12 specimens were tested for each formulation, and the reported thermal conductivity values represent the mean across all tested specimens.

Raman spectroscopy was used to evaluate the graphitic structure and relative defect content of the graphite intercalated compounds and expanded graphite fillers. Raman spectra were collected using an inVia™ confocal Raman microscope (Renishaw, UK) equipped with a 532 nm laser and a 50× objective. Spectra were collected over the range of 300–1600 cm^{-1} with a spectral resolution of approximately 1.5 cm^{-1}. For each measurement location, spectra were acquired using four accumulations with an acquisition time of 10 s per accumulation. The laser power at the sample was set to 100%. Prior to measurement, the spectrometer was calibrated using the Si peak at 520.5 cm^{-1}. The I_D/I_G ratio was calculated after baseline correction using the peak heights of the D band near 1330 cm^{-1} and the G band near 1572 cm^{-1}.

Morphological characterization of the expanded graphite fillers was performed using high-resolution field emission environmental scanning electron microscopy (Quattro S FE-ESEM, Thermo Fisher Scientific, USA). Imaging was conducted in secondary electron (SE) mode at an accelerating voltage of 20 kV. The samples were mounted on carbon tape and imaged without any additional conductive coating.

X-ray powder diffraction (XRD) was used to characterize the crystal structure of the graphite intercalated compounds and expanded graphite fillers. XRD spectra were collected at room temperature using a Rigaku SmartLab diffractometer (Rigaku Corporation, Japan) with Cu Kα radiation ((\lambda = 1.5406) Å). The instrument was operated at 40 kV and 30 mA. Data were collected using the Bragg–Brentano configuration over a 2(\theta) range of 5–80° with a step size of 0.02°.

X-ray photoelectron spectroscopy (XPS) was used to determine the surface elemental composition of the GIC and EG samples. Survey spectra were collected using a Thermo Scientific K-Alpha instrument equipped with a monochromated Al Kα X-ray source ((h\nu = 1486.6) eV) and a 400 µm spot size. Charge neutralization was used as needed during analysis. Binding energies were referenced to the C 1s peak at 284.8 eV. Survey spectra were acquired at a pass energy of 200 eV with an effective acquisition time of approximately 272 s per sample. For each sample, 20 scans were averaged at one location. Elemental atomic percentages of carbon, oxygen, and sulfur, along with the C/O ratios, were quantified using the instrument sensitivity factors in Avantage software.

3.3 Results and Discussion

3.3.1 Reaction Time Optimization Study for H_2O_2-Based EG Intercalation

The H_2O_2/H_2SO_4 intercalation route was optimized by evaluating the effect of reaction time on the thermal transport performance of epoxy/H_2O_2-EG composites. For this optimization study, the H_2SO_4:H_2O_2 volume ratio was kept constant at 4:1, while two acid/oxidant combinations were compared: 24 mL H_2SO_4 with 6 mL H_2O_2 and 20 mL H_2SO_4 with 5 mL H_2O_2. The graphite intercalated compounds obtained from these reactions were thermally expanded to form H_2O_2-derived expanded graphite, which was then incorporated into epoxy at 10wt% loading. The 10wt% loading was used as the screening composition to identify the reaction condition that produced the most effective expanded graphite filler for thermal transport.

Figure 3.6 shows the through-thickness thermal diffusivity of epoxy/H_2O_2-EG composites prepared using different H_2O_2/H_2SO_4 reaction times. The thermal diffusivity values show that the reaction time has a clear influence on the resulting composite performance. For the 24 mL H_2SO_4/6 mL H_2O_2 condition, thermal diffusivity increased with reaction time up to approximately 5–6 min, after which a reduction was observed at longer reaction time. The highest average thermal diffusivity was approximately 5.3 $mm^2\ s^{-1}$ for both the 5 min and 6 min reactions. However, the 6 min reaction resulted in higher thermal conductivity value.

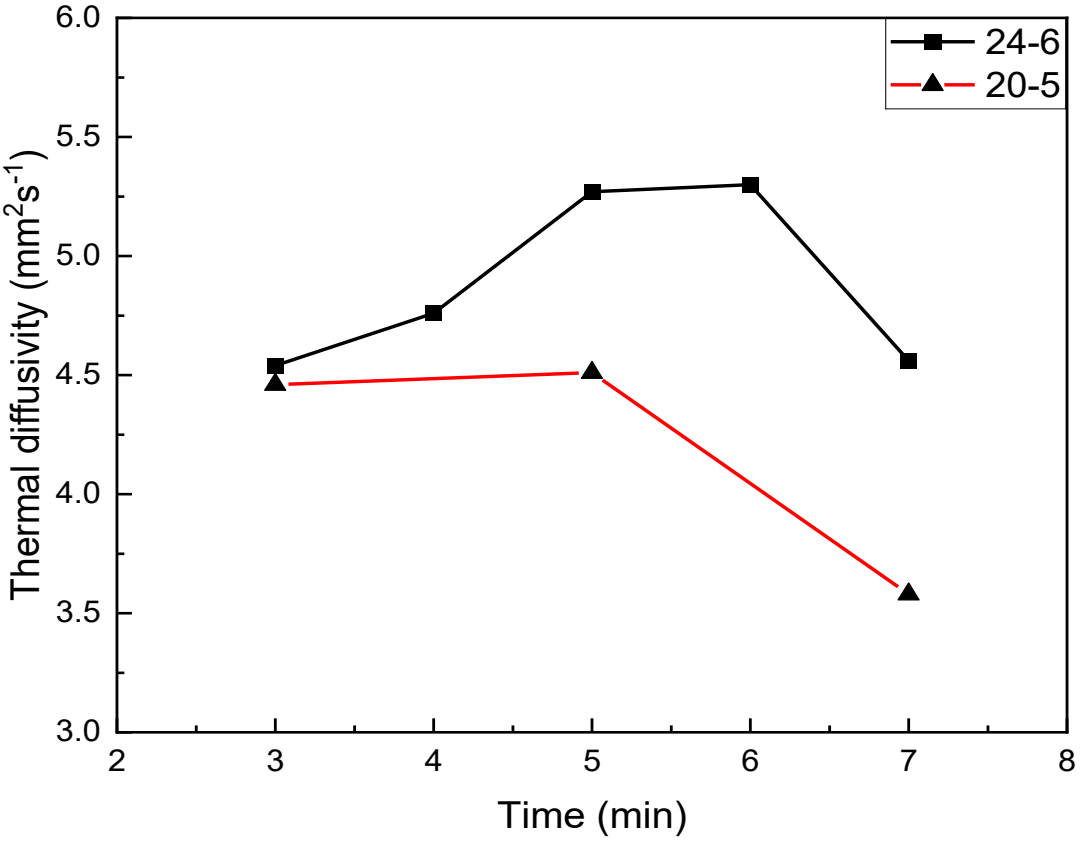


Figure 3.6 Optimization of reaction time for thermal diffusivity enhancement of epoxy/EG composites (H_2SO_4:H_2O_2 = 4:1)

The improvement in thermal diffusivity with increasing reaction time up to the optimum condition can be attributed to more effective graphite intercalation and subsequent expansion. At short reaction times, the intercalation process may be incomplete, limiting the extent of expansion during thermal treatment. Incomplete intercalation can reduce the ability of the expanded graphite to form continuous graphitic pathways in the epoxy matrix. As a result, heat transport remains more dependent on isolated filler-filler contacts and polymer-rich regions, which limits the composite thermal diffusivity.

In contrast, when the reaction time is increased to the optimized range, the H_2O_2/H_2SO_4 mixture can more effectively intercalate the graphite structure. This promotes expansion during the high-temperature treatment and can produce expanded graphite with improved filler connectivity in the epoxy matrix. The resulting graphitic network provides more efficient pathways for heat transport through the composite. Therefore, the increase in thermal diffusivity from shorter reaction times to the 5–6 min range suggests that sufficient intercalation and expansion are necessary for achieving high thermal transport performance.

However, further increasing the reaction time does not continue to improve the thermal diffusivity. The reduction observed at longer reaction time suggests that excessive exposure to the acidic oxidizing environment may negatively affect the expanded graphite structure. Longer reaction times can increase the possibility of graphitic lattice damage, flake fragmentation, or excessive oxidation. These effects may reduce the intrinsic quality of the graphitic filler or disrupt the formation of continuous graphitic pathways in the epoxy matrix. Therefore, the reaction must be controlled to balance sufficient intercalation with preservation of the graphitic structure[30].

The comparison between the two H_2SO_4/H_2O_2 volume combinations further shows that the 24 mL H_2SO_4/6 mL H_2O_2 condition produced higher thermal diffusivity than the 20 mL H_2SO_4/5 mL H_2O_2 condition. Although both reactions used the same 4:1 acid-to-oxidant volume ratio, the higher total amount of acid and oxidizing agent in the 24 mL/6 mL condition appears to provide a more effective intercalation environment for the graphite flakes. This indicates that both the relative ratio and the absolute quantity of the reactants can influence GIC formation, expansion behavior, and final composite thermal transport.

Based on these results, the 24 mL H_2SO_4/6 mL H_2O_2 reaction for 6 min was selected as the optimized H_2O_2 intercalation condition for further epoxy/H_2O_2-EG composite preparation. This condition provided the best balance between reaction time, intercalation effectiveness, and thermal diffusivity performance. The optimized H_2O_2-EG filler was therefore used for the subsequent filler-loading study, where epoxy/H_2O_2-EG composites were prepared at different EG weight fractions.

The incorporation of H_2O_2-derived EG led to a substantial increase in thermal conductivity compared with pristine epoxy. As shown in Figure 3.7, the thermal conductivity increased with increasing EG loading up to 10wt%, where a maximum value of 5.15 W m^{-1} K^{-1} was obtained. At higher EG loadings, a slight decrease in thermal conductivity was observed.

The increase in thermal conductivity up to 10wt% EG indicates that the H_2O_2-derived expanded graphite was effective in forming thermally conductive pathways within the epoxy matrix. This behavior is consistent with the role of expanded graphite as a graphitic filler that can provide more efficient heat-conduction pathways than the neat polymer alone. As filler loading increases, the probability of contact and overlap between expanded graphite particles also increases, which can improve graphitic network formation and enhance heat transport through the composite.

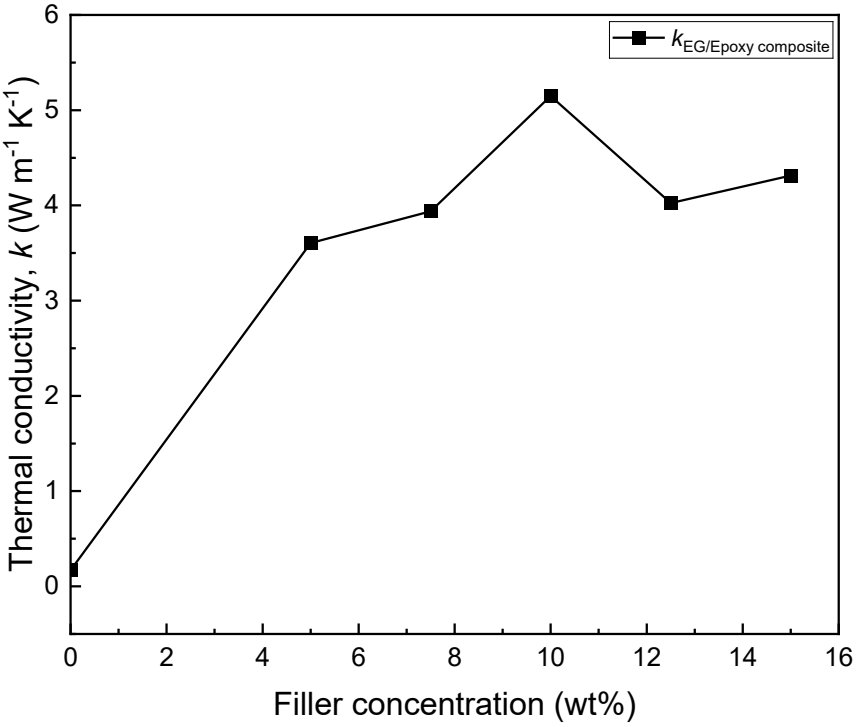


Figure 3.7 Epoxy/EG composite thermal conductivities (k) values at 5, 7.5, 10, 12.5, 15wt% filler concentration

However, the decrease in thermal conductivity beyond 10wt% suggests that increasing filler loading does not necessarily lead to continuous improvement. The literature suggests that at higher EG concentrations, factors such as filler crowding, non-uniform packing, reduced resin infiltration, void formation, or disruption of the expanded graphite structure during mixing may limit further enhancement[80-84]. The samples prepared with 12.5 and 15wt% fillers exhibited poor composite structural integrity compared to samples with lower filler concentrations. It was observed that at these concentrations, the filler volume was substantially high, and the epoxy was insufficient to compactly bond the fillers together. After curing, the 15wt% sample also exhibited a flexible characteristic. Such reduced structural integrity likely weakened both filler-filler contact quality and filler-matrix bonding, thus increasing the interfacial and contact resistance of the material leading to loss in thermal transport as evident from the results[8,80-82,85]. Therefore, the

optimum filler loading for the epoxy/H_2O_2-EG system was identified as 10wt% under the processing conditions used in this study.

3.3.2 Raman Analysis

Raman spectroscopy was used to evaluate the structural quality of the graphite precursor, graphite intercalated compounds (GICs), and expanded graphite (EG) fillers prepared using different H_2O_2/H_2SO_4 intercalation conditions. For graphitic materials, the G band is associated with the in-plane vibration of sp^2-bonded carbon atoms, while the D band is commonly associated with disorder-induced scattering caused by defects, edges, or disruption of the graphitic lattice. The ratio of the D-band intensity to the G-band intensity, I_D/I_G, is therefore often used as an indicator of the relative defect density in graphite-based materials. In general, a lower I_D/I_G ratio suggests better preservation of the graphitic structure, while a higher value indicates greater defect content or structural disorder[86,87]. Analyzing the defects in graphitic materials through Raman spectroscopy is essential as it negatively affects its intrinsic thermal conductivity through enhanced phonon scattering[88-90].

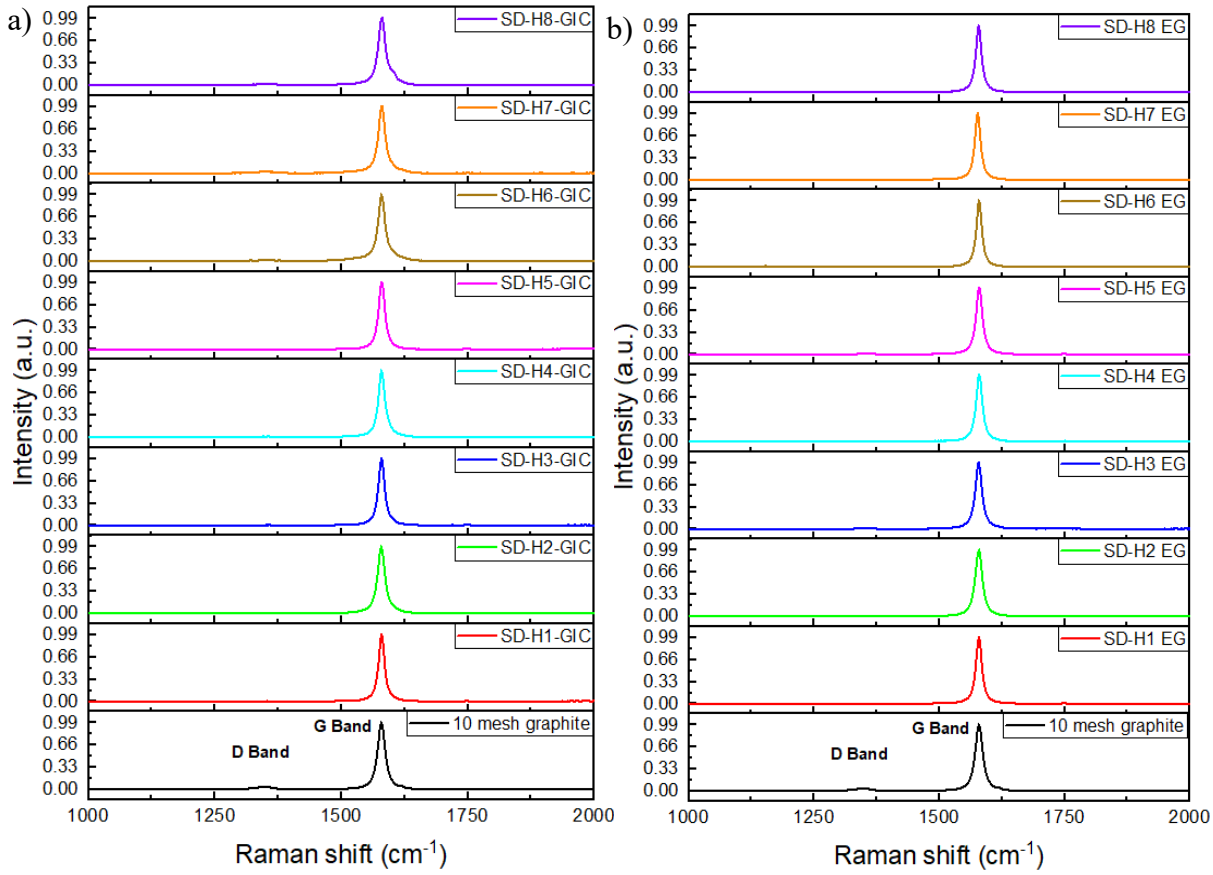


Figure 3.8: Raman survey spectra of a) GIC and b) EG fillers synthesized during reaction-time optimization for epoxy/EG composite study

The Raman spectras for the EG fillers and ther corresponding GICs are shown in figure 3.8. Table 3.3 summarizes the D-band position, G-band position, and I_D/I_G ratio for the starting graphite, GICs, and EG fillers prepared under the different H_2O_2-based intercalation conditions. The starting 10 mesh graphite showed a D band at 1350.02 cm^{-1}, a G band at 1578.82 cm^{-1}, and an I_D/I_G ratio of 0.03849. After intercalation and thermal expansion, the G band for most GIC and EG samples remained close to 1578–1581 cm^{-1}, indicating that the primary graphitic structure was still present after chemical treatment and thermal expansion. The D band appeared between approximately 1326 and 1358 cm^{-1}, depending on the sample.

Table 3.3 Raman D and G band positions with I_D/I_G ratios for graphite, GIC and EG samples during reaction time optimization

Sample name	D band (cm^{-1})	G band (cm^{-1})	I_D/I_G ratio
10 Mesh Graphite	1350.02148	1578.82031	0.03849
SD_H1 EG	1335.14258	1579.60156	0.001070
SD_H1 GIC	1352.62695	1578.82031	0.006780
SD_H2 EG	1348.1875	1579.60156	0.003950
SD_H2 GIC	1344.80859	1578.82031	0.010950
SD_H3 EG	1355.82813	1578.98047	0.014580
SD_H3 GIC	1352.62695	1578.82031	0.009120
SD_H4 EG	1349.03516	1578.98047	0.012580
SD_H4 GIC	1355.23242	1578.82031	0.014790
SD_H5 EG	1355.76758	1580.01367	0.011690
SD_H5 GIC	1342.19922	1578.82031	0.002740
SD_H6 EG	1326.33789	1578.98047	0.002620
SD_H6 GIC	1352.62695	1578.82031	0.023460
SD_H7 EG	1353.56445	1576.80078	0.001280
SD_H7 GIC	1350.02148	1578.82031	0.032380
SD_H8 EG	1350.16797	1578.98047	0.012580
SD_H8 GIC	1357.83789	1581.35547	0.025200

The I_D/I_G ratios of the H_2O_2-derived EG samples were generally low, indicating that the expanded graphite fillers retained a substantial degree of graphitic structural integrity after processing. Among the EG samples, SD_H1 EG, SD_H7 EG, SD_H6 EG, and SD_H2 EG showed particularly low I_D/I_G ratios of 0.00107, 0.00128, 0.00262, and 0.00395, respectively. These values suggest that these EG samples had relatively low Raman-detectable defect content. In comparison, SD_H4 EG, which produced the highest composite thermal conductivity, showed an I_D/I_G ratio of 0.01258. Although this value is still low in absolute terms, it is not the lowest among the EG fillers.

This result is important because it shows that Raman-based defect analysis alone cannot fully determine which expanded graphite filler will produce the highest thermal conductivity in epoxy. If the I_D/I_G ratio were the only controlling factor, the samples with the lowest defect ratios

would be expected to provide the highest composite thermal conductivity. However, the best-performing filler in the composite was SD_H4 EG, despite not having the lowest I_D/I_G ratio. Therefore, while preservation of graphitic structure is important, it is only one factor influencing the final thermal transport performance.

The thermal conductivity of epoxy/EG composites depends on several structural and processing-related factors in addition to graphitic defect density. A filler with a very low I_D/I_G ratio may retain high intrinsic graphitic quality, but if it does not expand effectively, form a connected network, or disperse favorably in the epoxy matrix, the composite thermal conductivity may still be limited. Conversely, a filler with slightly higher Raman-detectable disorder may produce better composite performance if it forms more continuous and better-connected graphitic pathways.

The GIC samples showed greater variation in I_D/I_G ratio than the EG samples. For example, SD_H7 GIC and SD_H8 GIC showed relatively higher I_D/I_G ratios of 0.03238 and 0.02520, respectively, while SD_H5 GIC showed a much lower value of 0.00274. These variations indicate that the intercalation conditions influenced the structural state of the graphite prior to expansion. However, the relationship between GIC defect ratio and final EG composite performance is not direct, because the subsequent thermal expansion step can strongly affect filler morphology, expansion volume, and network-forming ability.

Overall, the Raman results confirm that the H_2O_2/H_2SO_4 intercalation and expansion process produced EG fillers that largely retained graphitic structure, as indicated by the presence of clear G bands and generally low I_D/I_Gratios. However, the optimized SD_H4 EG sample demonstrates that the best thermal conductivity performance cannot be assigned solely to the

lowest defect ratio. Raman spectroscopy provides useful information about structural integrity, but it must be interpreted together with thermal conductivity data, expansion behavior, morphology, and composite processing effects. Therefore, the enhanced thermal conductivity of the optimized epoxy/H_2O_2-EG composite is attributed to the combined effect of retained graphitic structure and favorable network formation within the epoxy matrix, rather than Raman-derived defect density alone.

3.3.3 X-ray Photoelectron Spectroscopy Analysis

X-ray photoelectron spectroscopy (XPS) was used to evaluate the surface elemental composition of the graphite precursor, graphite intercalated compounds (GICs), and the corresponding expanded graphite (EG) fillers. The survey spectra in Figure 3.9 show the characteristic C 1s and O 1s peaks near 284–285 eV and 532 eV, respectively, confirming the dominant presence of carbon and oxygen in the samples. Trace amounts of sulfur were also observed in several GIC and EG samples, which is expected because sulfuric acid was used as the intercalating medium during the H_2O_2/H_2SO_4 reaction. This XPS analysis is based on a survey spectra and hence should primarily be considered in terms of relative surface oxidation rather than detailed functional group specification.

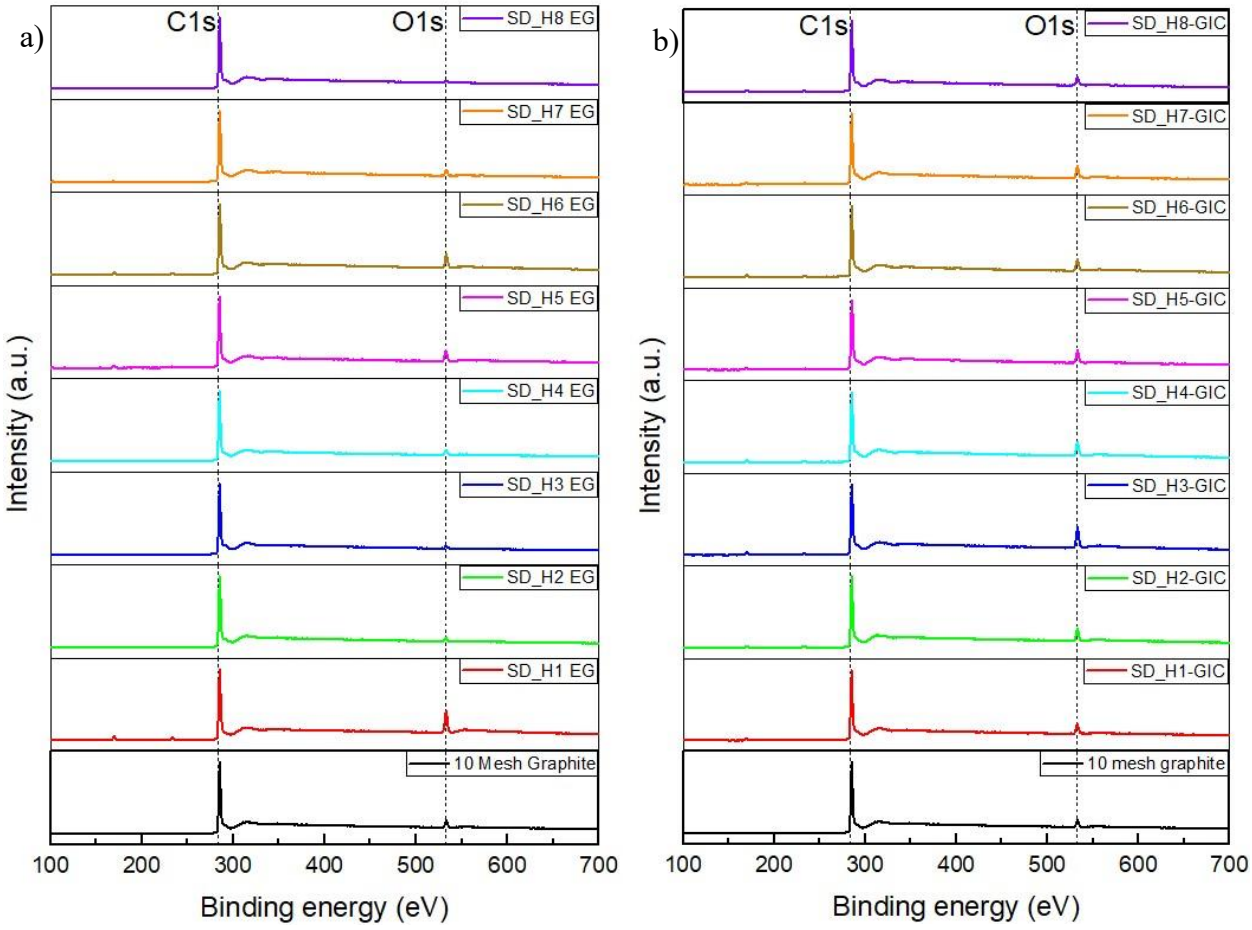


Figure 3.9 XPS survey spectra of a) EG and b) GIC fillers synthesized during reaction-time optimization for epoxy/EG composites, showing characteristic C 1s (~285 eV) and O 1s (~532 eV) peaks

The C/O ratio is an important parameter for graphite-based fillers because it provides an estimate of the relative oxygen content introduced during chemical treatment. A higher C/O ratio generally indicates lower oxygen content and better preservation of the carbon-rich graphitic structure. In contrast, a lower C/O ratio suggests a higher degree of oxidation, which may be associated with the introduction of oxygen-containing functional groups. While some oxygen-containing groups can assist intercalation or influence interaction with the polymer matrix, excessive oxidation can disrupt the sp^2 carbon network and introduce structural defects that reduce

the intrinsic thermal conductivity of graphitic fillers. Therefore, the C/O ratio is commonly used as one indicator of the chemical and structural state of chemically treated graphite[30,82].

Table 3.4 XPS elemental composition (atomic %) and corresponding C/O ratios for GICs and EG fillers synthesized using different reaction times for epoxy/EG composites. The results support the evaluation of intercalation efficiency and thermal performance correlation

Samples	**Atomic Composition by XPS (atomic %)**			**C/O ratio**
	C (~284 eV)	**O (~532 eV)**	**S (~169 eV)**	
10 mesh graphite	93.52	5.34	1.13	17.51
SD_H1 EG	83.43	13.71	2.86	6.08
SD_H1-GIC	*91.53*	*7*	*1.46*	*13.07*
SD_H2 EG	97.05	2.7	0.25	35.94
SD_H2-GIC	*90.16*	*8.38*	*1.46*	*10.76*
SD_H3 EG	97.89	2.11	-	46.39
SD_H3-GIC	*85.29*	*11.86*	*2.03*	*7.19*
SD_H4 EG	96.26	3.74	-	25.74
SD_H4-GIC	*89.87*	*8.54*	*1.59*	*10.52*
SD_H5 EG	92.39	6.04	1.57	15.30
SD_H5-GIC	*92.24*	*6.11*	*1.65*	*15.10*
SD_H6 EG	89.66	8.82	1.53	10.16
SD_H6-GIC	*90.36*	*7.96*	*1.68*	*11.35*
SD_H7 EG	95.3	4.38	0.33	21.76
SD_H7-GIC	*89.91*	*8.41*	*1.68*	*10.69*
SD_H8 EG	98.44	1.56	-	63.10
SD_H8-GIC	*92.74*	*5.86*	*1.41*	*15.82*

The XPS results seen in table 3.4 show that, in general, the EG samples had higher C/O ratios than their corresponding GIC samples. This trend can be attributed to the loss or decomposition of oxygen-containing groups and intercalated species during the high-temperature thermal expansion step. The reduction in oxygen content after expansion suggests partial removal of oxidized groups from the graphite structure, which is consistent with the conversion of GICs into more carbon-rich expanded graphite. In addition, sulfur content was reduced or absent in

several EG samples, indicating that sulfur-containing intercalated species were also removed during thermal expansion.

Among the EG fillers, the C/O ratio varied considerably depending on the intercalation condition. For example, SD_H8 EG showed the highest C/O ratio of 63.10, followed by SD_H3 EG and SD_H2 EG with C/O ratios of 46.39 and 35.94, respectively. In comparison, SD_H4 EG, which produced the highest thermal conductivity in the epoxy composite, had a C/O ratio of 25.74. Although this value indicates a relatively carbon-rich structure, it was not the highest among the EG samples. This result shows that the filler producing the best composite thermal conductivity was not simply the filler with the highest C/O ratio.

The optimized SD_H4 EG sample likely provided a more favorable balance between chemical composition and physical structure. Its C/O ratio suggests that the filler retained a substantial carbon-rich graphitic structure after expansion, while its superior composite thermal conductivity indicates that it may have also formed more effective heat-conduction pathways within the epoxy matrix. Thus, the performance of SD_H4 EG should be interpreted as the combined result of sufficient graphitic structural preservation and favorable network formation, rather than the result of C/O ratio alone.

Overall, the XPS results confirm that the H_2O_2/H_2SO_4 intercalation and thermal expansion process modified the surface chemistry of graphite and produced EG fillers with varying oxygen and sulfur contents. The generally higher C/O ratios of EG samples relative to GICs suggest removal of oxygen-containing and sulfur-containing species during thermal expansion. However, similar to the Raman analysis, the XPS results demonstrate that a single characterization parameter cannot fully explain the thermal conductivity behavior of epoxy/EG composites. The C/O ratio

provides useful insight into the oxidation state of the filler, but it must be considered together with Raman structural analysis, expansion behavior, morphology, filler network formation, and composite processing effects.

3.3.4 X-ray Diffraction Analysis

X-ray diffraction (XRD) was used to evaluate the interlayer spacing and graphitic stacking structure of the graphite precursor, graphite intercalated compounds (GICs), and expanded graphite (EG) fillers. For graphitic materials, the characteristic (002) diffraction peak is typically observed near $2\theta \approx 26.5°$, corresponding to an interlayer spacing of approximately 3.35 Å[91]. In the present study, the 10-mesh graphite precursor exhibited a strong (002) peak at approximately $2\theta \approx 26.3°$, corresponding to a d-spacing of 3.38 Å. This value closely matches the expected interlayer spacing of graphitic materials, confirming the ordered graphitic stacking structure of the starting material.

After the H_2O_2/H_2SO_4 intercalation reaction, the GIC samples generally exhibited broadened and lower-angle features in the (002) region compared with the 10-mesh graphite precursor. The shift of several GIC peaks toward lower 2θ values correspond to an increase in d-spacing, which is consistent with intercalation-induced expansion of the graphite galleries. For example, as seen in figure 3.10 and table 3.5, SD_H1 GIC, SD_H3 GIC, SD_H5 GIC, SD_H6 GIC, and SD_H8 GIC showed (002)-region peaks at lower angles than the graphite precursor, with d-spacing values ranging from approximately 3.43 to 3.56 Å. This increase in interlayer spacing indicates that the H_2O_2/H_2SO_4 reaction introduced intercalated species between graphite layers and disrupted the regular graphitic stacking arrangement.

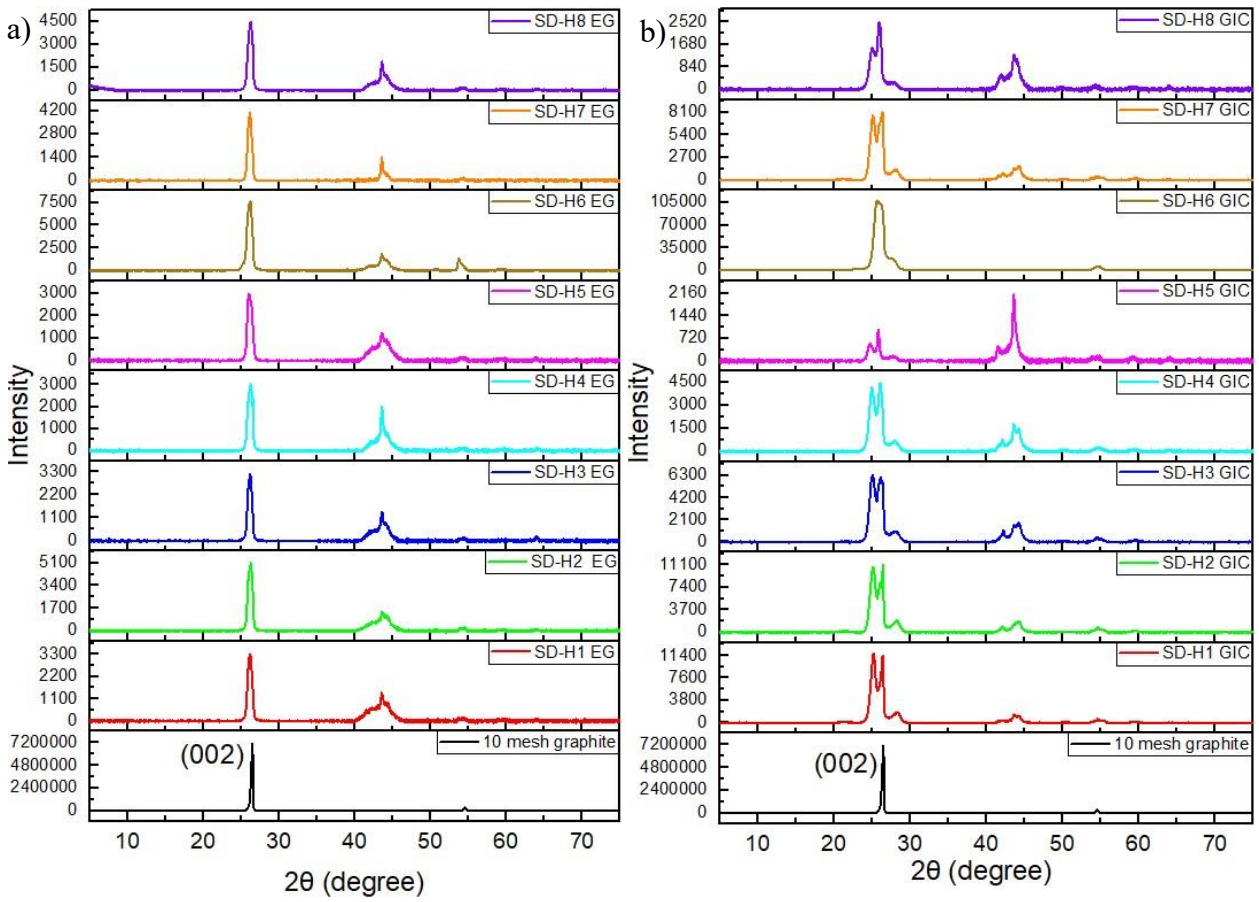


Figure 3.10: XRD patterns of a) EG and b) GIC fillers synthesized using fixed intercalant volume ratio (H_2SO_4:H_2O_2 = 4:1) with varying reaction times for epoxy/EG composites

The broadening of the GIC diffraction features also suggests that the intercalation process introduced structural disorder or reduced stacking coherence within the graphite particles. This behavior is expected for graphite intercalated compounds because the insertion of molecular or ionic species between graphene layers can create a distribution of local interlayer spacings rather than a single highly ordered graphite-like spacing. Therefore, the lower-angle and broadened (002)-region features provide evidence that the graphite structure was chemically modified during the intercalation step.

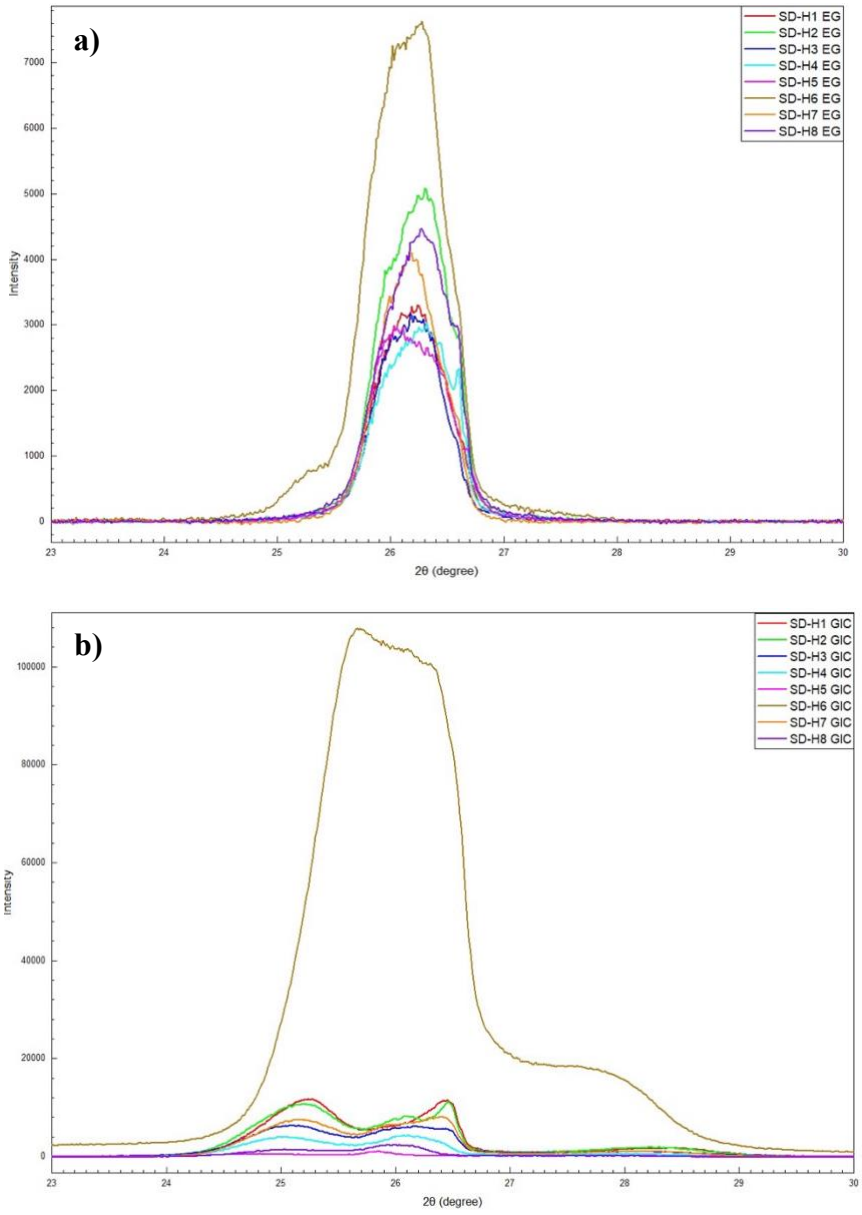


Figure 3.11 Inset of XRD spectra of a) EG and b) GIC samples showing peak broadening and shifting in the (002) reflection during reaction-time optimization for epoxy/EG composites

The EG samples showed sharper (002) reflections closer to the graphite precursor position. This recovery of the (002) peak near $2\theta \approx 26.2°$ indicates partial restoration of graphitic stacking after removal or decomposition of intercalated species during high-temperature expansion. The EG

samples generally had d-spacing values near 3.38–3.41 Å, suggesting that the expanded graphite retained or recovered graphitic order after thermal treatment. This result is consistent with the conversion of GICs into expanded graphite, where the intercalated species drive expansion but are largely removed during rapid heating.

The thermally optimized filler, SD_H4 EG, showed a recovered (002) peak near $2\theta \approx 26.316°$, corresponding to a d-spacing of approximately 3.38 Å. This indicates substantial restoration of graphitic stacking after the thermal expansion step. The recovery of the (002) reflection suggests that SD_H4 EG retained a graphitic structure suitable for thermal transport, which is important because graphitic stacking and preservation of sp^2 carbon networks contribute to efficient phonon transport within the filler.

Table 3.5 XRD-derived 2θ and corresponding d-spacing values for graphite, GICs, and EG fillers synthesized using fixed intercalant volume ratio (H_2SO_4:H_2O_2 = 4:1) with varying reaction times (reaction-time optimization phase) for epoxy/EG composites.

Sample name	**2 θ (°)**	**d-spacing (*Å*)**
SD_H1 EG	26.238	3.39
SD_H1 GIC	*25.198*	*3.53*
SD_H2 EG	26.303	3.38
SD_H2 GIC	*26.459*	*3.36*
SD_H3 EG	26.173	3.40
SD_H3 GIC	*25.094*	*3.54*
SD_H4 EG	26.316	3.38
SD_H4 GIC	*26.108*	*3.41*
SD_H5 EG	26.095	3.41
SD_H5 GIC	*25.848*	*3.44*
SD_H6 EG	26.277	3.38
SD_H6 GIC	*25.692*	*3.56*
SD_H7 EG	26.186	3.40
SD_H7 GIC	*26.407*	*3.37*
SD_H8 EG	26.277	3.38
SD_H8 GIC	*25.926*	*3.43*

However, SD_H4 EG does not appear uniquely superior based on XRD alone. Several other EG samples also showed recovered (002) peaks near the graphite position and similar d-spacing values. For example, SD_H2 EG, SD_H6 EG, and SD_H8 EG also exhibited d-spacing values close to 3.38 Å. Therefore, although XRD confirms that SD_H4 EG retained graphitic stacking after expansion, the XRD results alone do not fully explain why SD_H4 EG produced the highest epoxy composite thermal conductivity.

This observation is consistent with the Raman and XPS results discussed earlier. Each characterization method provides useful information about a specific aspect of the filler structure or chemistry, but no single parameter fully determines the composite thermal conductivity. The optimized thermal performance of SD_H4 EG should therefore be interpreted as the result of a favorable combination of factors, including recovered graphitic stacking, retained structural integrity, suitable degree of expansion, filler morphology, network formation, and processing behavior in the epoxy matrix[81-84].

Overall, the XRD results confirm that the H_2O_2/H_2SO_4 intercalation process increased the interlayer spacing and disrupted the ordered stacking of the graphite precursor, while the subsequent thermal expansion step partially restored graphite-like (002) reflections in the EG fillers. The SD_H4 EG sample showed substantial recovery of graphitic stacking, but its superior thermal conductivity performance should be viewed as part of an experimentally identified optimum processing window rather than the direct result of maximizing a single XRD-derived structural descriptor.

3.3.5 GIC and EG structure and morphology

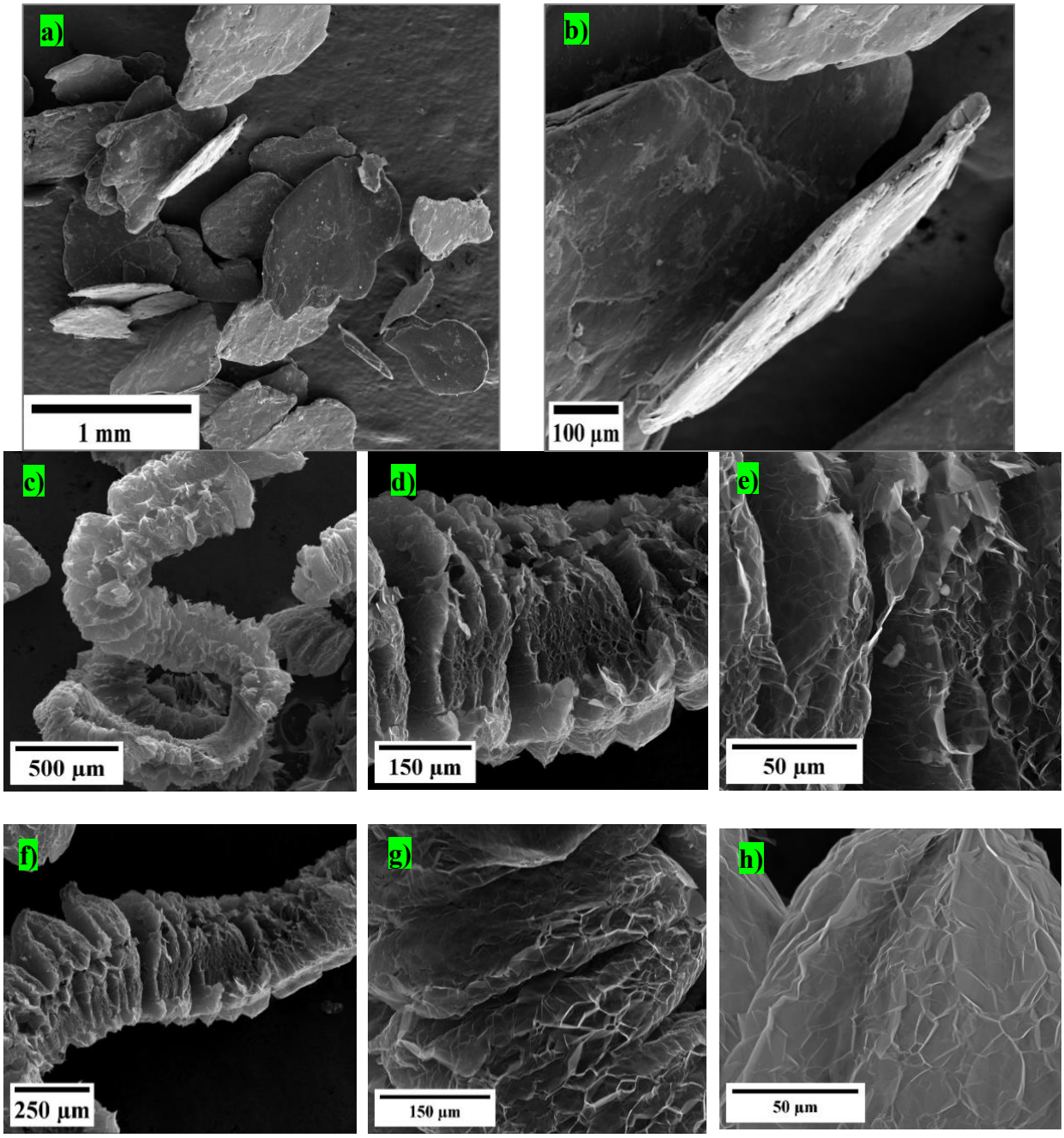


Figure 3.12. FE-ESEM images of 10 mesh graphite a) 35X and b) 150X and FE-ESEM micrographs of the optimized expanded graphite (SD-H4 EG) used in the epoxy/EG composite, captured at various magnifications: (c) 50×, (d) 150×, (e) 1000×, (f) 86×, (g) 350×, and (h) 1000×

The graphite precursor and the optimized expanded graphite (EG) filler were further characterized for its morphology using Field-Emission Environmental Scanning Electron Microscopy (FE-ESEM). The corresponding micrographs are shown in figure 3.12. As seen in the figure 3.12a and 3.12b, the 10-mesh graphite precursor consists of tightly stacked layers, without any pores or expansion prior to the intercalation process.

Figures 3.12c-h correspond to micrographs of the optimized expanded graphite filler, SD-H4 EG, taken at various magnifications. The filler exhibits a wrinkled lamellae morphology along with interconnected porous regions. These porous regions result from uneven expansion of the intercalated graphite precursor at high temperatures and are important in forming interpenetrating graphene-epoxy networks. During the composite processing, it is important to preserve the interconnected lamellar microstructures as they contribute towards formation of thermal pathways essential to achieve high composite thermal conductivity[14,92,93].

Overall, these micrographs from FE-ESEM, confirm the successful thermal expansion of the graphite precursor. The morphologies shown confirm that the filler demonstrates the characteristics expected from EG.

3.4 Conclusion

This chapter investigated the use of expanded graphite as a filler to improve the filler connectivity for enhancing the thermal transport in epoxy-based composites. -10-mesh graphite precursor was subjected to H_2O_2/H_2SO_4 intercalation reaction to synthesize intercalated graphite compounds (GIC), which was then followed by a thermal expansion to produce expanded graphite. The study

focused on optimizing the intercalation reaction times and how the resulting EG fillers affected the through-plane thermal conductivity of epoxy-EG composites.

For the scope of this study, a fixed volume ratio of 4:1 was used for H_2SO_4 : H_2O_2 in the optimization process. Two different absolute volume pairs were studied for optimizing the reaction time. Among the tested combinations, 24ml H_2SO_4 : 6ml H_2O_2 condition with a 6 minute reaction time, corresponding to the SD_H4 formulation provided the best balance between intercalation effectiveness, expansion behavior and thermal transport performance in the epoxy/EG composite.

The optimized H_2O_2- EG filler was further used to prepare epoxy/EG composites at different filler loadings. The thermal conductivity of the composite increased with increasing EG loading upto 10wt%, following which a drop in thermal conductivity was observed. The maximum thermal conductivity seen at 10wt% was 5.15 $Wm^{-1}K^{-1}$. The drop in thermal conductivity after 10wt% suggests the dependency on a balance between improved graphitic network formation along with processing-related factors such as non-uniform packing, void formation or disruption in expanded structure morphology during the composite preparation.

Raman spectroscopy, XPS, and XRD were used to evaluate the structural and chemical characteristics of the GIC and EG fillers. Raman analysis showed that the ID/IG ratio provides useful information about graphitic defect content, but the optimized SD_H4 EG filler did not have the lowest ID/IG ratio among the samples. Similarly, XPS analysis showed that EG samples generally had higher C/O ratios than their corresponding GICs, consistent with removal of oxygen-containing species during thermal expansion; however, SD_H4 EG did not have the highest C/O ratio. XRD analysis confirmed that GIC samples generally showed broadened or lower-angle features associated with intercalation-induced changes in graphitic stacking, while EG samples

recovered (002) reflections near the graphite position after thermal expansion. The SD_H4 EG filler showed substantial restoration of graphitic stacking, but it was not uniquely superior based on XRD alone. These characterizations suggest the existence of an optimization window leading to favorable structural and chemical factors causing superior filler-filler connectivity. The findings from this chapter support the broader objective of improving epoxy composite thermal conductivity by controlling the internal structure and connectivity of graphitic fillers.

Chapter 4

Enhancement of Epoxy/Graphene Thermal Conductivity Through Graphene Alignment Using 3D Printing

4.1 Introduction

Graphene nanoplatelets (GnPs) are attractive fillers for thermally conductive epoxy composites because of their high aspect ratio and high in-plane thermal conductivity. However, this high intrinsic thermal conductivity is strongly anisotropic, with heat transport along the graphene basal plane being much more efficient than transport through the thickness direction. As a result, the orientation of GnPs within the epoxy matrix becomes an important factor in determining the direction and magnitude of heat transfer. In randomly oriented composites, many nanoplatelets are not aligned with the desired heat-flow direction, which limits the effective use of graphene's high in-plane thermal conductivity.

Filler alignment provides a route to improve directional thermal transport by orienting the high-conductivity direction of GnPs along the intended heat-spreading path. Several processing methods have been used to induce alignment in polymer composites, including shear mixing, mechanical pressing, field-assisted alignment, and extrusion-based processing. Among these approaches, paste-extrusion-based 3D printing is especially useful because it can combine material shaping with microstructural control. During extrusion through a nozzle, the platelets experience shear and geometric confinement, which can preferentially orient them along the flow direction.

After deposition, this orientation may be retained along the printed path, producing an anisotropic composite structure[94-98].

In paste-extrusion printing, nozzle geometry and printing speed can strongly influence both filler alignment and print quality. A longer nozzle can increase the residence time and shear history experienced by the epoxy/GnP paste, while a shorter nozzle may reduce pressure buildup and improve extrusion stability. While considering the nozzle shape, a rectangular nozzle can squeeze the paste into a wider and thinner shape, thus producing a flattened filament, which may promote in-plane orientation of GnPs along the print direction. However, these same processing conditions can also introduce challenges such as clogging and discontinuous extrusion due to air entrapment leading to void formation. Therefore, the nozzle geometry is an important factor in improving the thermal and electrical transport as it affects the filler alignment, and also the quality and continuity of the printed structure. Some studies have been performed to see the effect of nozzle geometry in filament based and direct ink writing 3d printing[99-102]. But studies on paste extrusion in combination with thermal and electrical transport are very limited.

In this chapter, paste-extrusion-based 3D printing is investigated as a method to induce GnP alignment in epoxy composites and improve directional in-plane thermal transport. A 9wt% epoxy/GnP paste was printed using a rectangular nozzle with a 3 mm × 1 mm outlet. The nozzle length was kept at 80 mm, and printing speeds of 750, 1000, 1250, and 1500 mm/min were tested. In-plane thermal conductivity is measured using the Angstrom method and electrical conductivity is measured using the four-probe method. The objective of this chapter is to determine how printing speed affect GnP alignment, and directional thermal and electrical transport in printed epoxy/GnP composites.

4.2 Materials and Experimental Methods

The epoxy system used in this chapter was the same as that used in Chapter 2. EPIKOTE RESIN MGS RIMR 135 was used as the epoxy resin, and EPIKURE CURING AGENT MGS RIMH 137 was used as the curing agent. Graphene nanoplatelets (GnPs) with an average thickness of approximately 6–8 nm and a lateral size of approximately 15 μm, purchased from Strem Chemicals, INC., were used as the thermally conductive filler. Acetone was used as the processing solvent to reduce the viscosity of the epoxy resin during mixing and to assist incorporation of GnPs into the resin before printing. Since this was a high GnP concentration mixture, use of acetone was sufficient. Acetone is also much easier to remove from the mixture and hence was the preferred choice of solvent in this study.

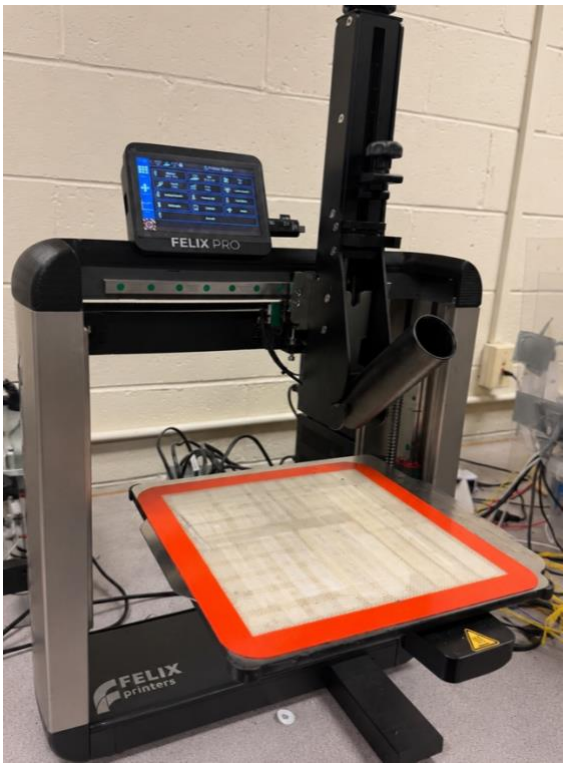


Figure 4.1 FELIX food 1.6 single head 3D printer

A 9 wt% epoxy/GnP composite paste was prepared using shear mixing. First, 40 g of epoxy resin was added to a beaker with acetone to prepare a total solution volume of 100 mL. GnPs were then added slowly into the epoxy/acetone solution to reduce the formation of large filler agglomerates during addition. The mixture was stirred using a mechanical shear mixer at 350 rpm while the beaker was maintained at 60 °C. Mixing was continued until acetone evaporated from the mixture and a concentrated epoxy/GnP paste was obtained. The beaker was then placed under vacuum to remove any residual acetone. After solvent removal, the curing agent was added to the epoxy/GnP mixture and manually mixed until a visually uniform printable paste was obtained.

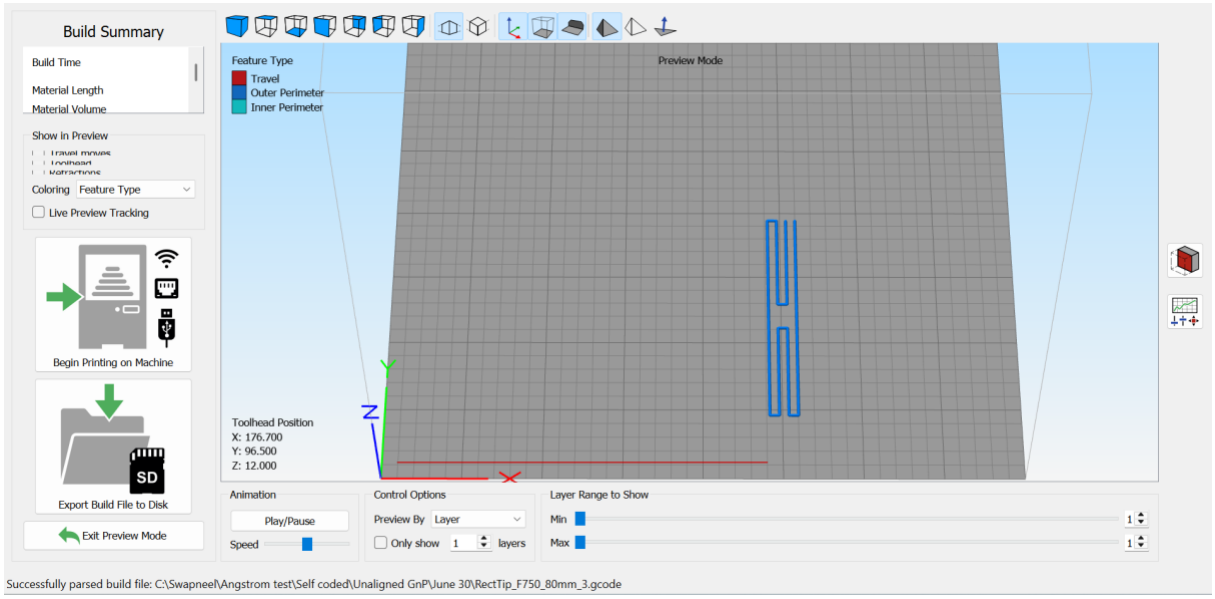


Figure 4.2 Visual representation of G-code in Simplify3D software

The epoxy/GnP samples were printed on FELIX Food 1.6 single-head 3D printer, as seen in figure 4.1. The printer uses a mechanical paste-extrusion configuration in which the material is extruded from a syringe through a nozzle and deposited along a programmed print path. Figure 4.3 shows the 80 mm long nozzle with a rectangular outlet dimension of 3 mm × 1.5 mm which was

used to print the composite paste. Printing was performed at four different print speeds: 750, 1000, 1250, and 1500 mm/min. The print bed was not heated during deposition. After printing, the bed was heated to 60°C to cure the printed epoxy/GnP samples.

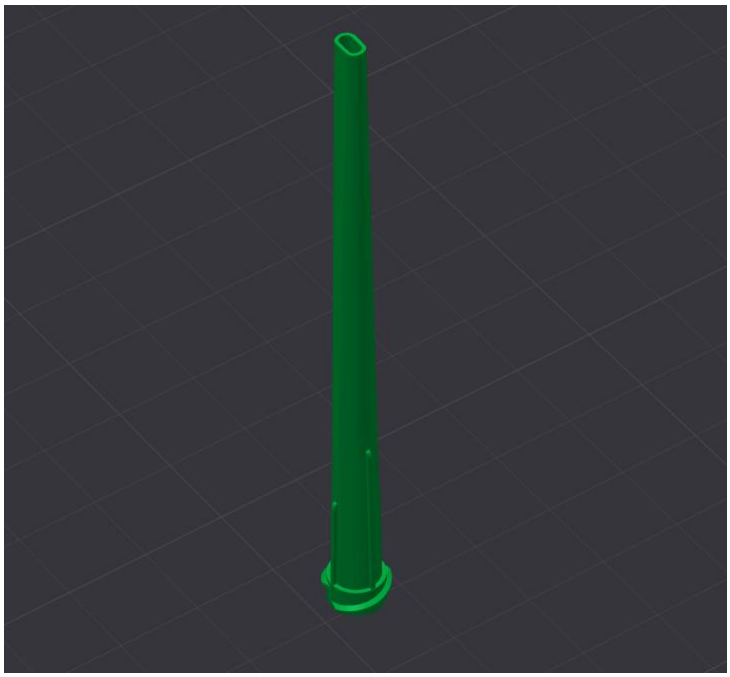


Figure 4.3 Nozzle used to print the epoxy/GnP samples

For the in-plane thermal conductivity measurements, rectangular samples of 80 mm length and 12 mm width were printed. For incorporating the heating wire into the sample, a rectangular notch was designed into the sample design. For 3d printing, custom G-codes were written for each sample and tested for accuracy using the Simplify3D software as seen in figure 4.2. Once the printed samples cured, a 21 Ω per feet resistance heating wire was coiled into the notch evenly. To maintain consistent heating, a constant length of two feet of the resistance heating wire was used for all samples. The wire was then coated with a thermally conductive paste to ensure proper contact between the wire and the samples as seen in figure 4.4.

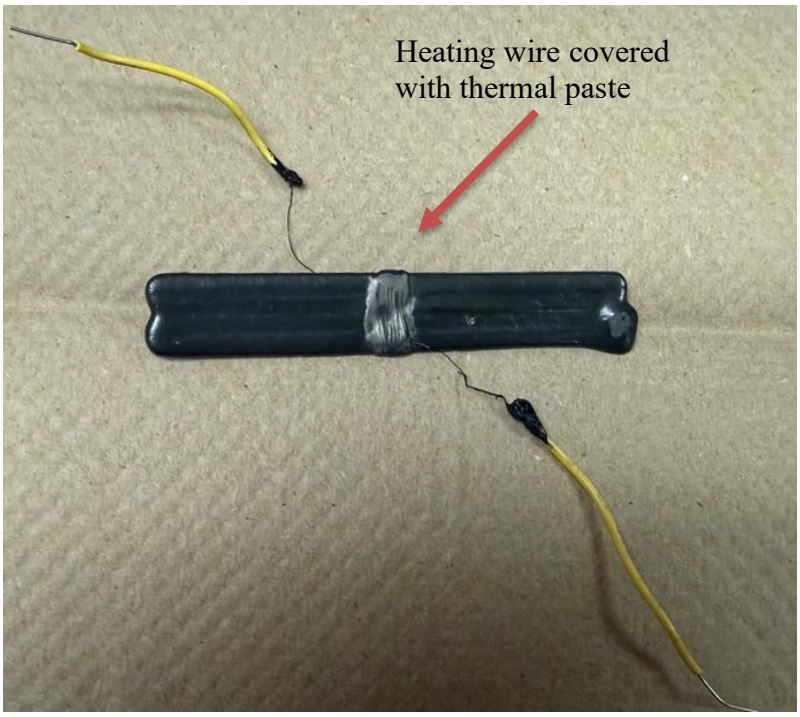


Figure 4.4 3D printed sample with attached heating wire

In-plane thermal transport of the printed epoxy/GnP composites was measured using the Angstrom method. The setup, seen in figure 4.5, primarily includes a vacuum chamber to hold the sample under vacuum to minimize convection losses and a FLIR infrared camera coupled with the data recording software to record the temperature change during the measurements. A sample holder, shown in figure 4.6, was used to hold the sample inside the vacuum chamber. The sample holder also functioned as a reference for setting up the locations of the 6 cursors used for measurements. Additional details of the Angstrom measurement setup and calculations are discussed in the following section.

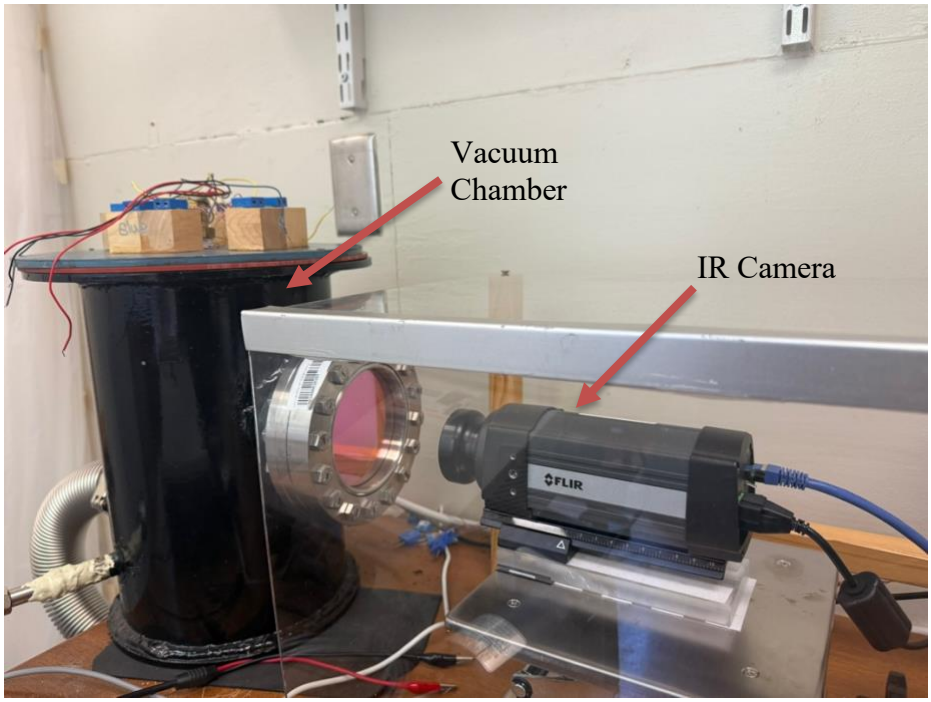


Figure 4.5 Angstrom method setup for in-plane thermal diffusivity measurement

To further analyze the effect of printing speed on filler alignment, the 3d printed epoxy/GnP samples were tested for in-plane electrical conductivity using the four-point probe setup. Keithley Multimeter 2100 was coupled with an in-house built four-point probe setup to measure the resistance of the printed samples. This resistance was further used to calculate the volume resistivity using the equation

$$\rho = \frac{R\,A}{L} \tag{4.1}$$

Where R is the resistance, A is the cross-sectional area of the printed sample, and L is the length of sample used to measure the resistance. It is important to note that the resistance measurement for each sample was taken on either side of the heating wire and then averaged to obtain the final

resistance value. This method avoids the interference of the heating wire in the resistance measurements. The volume resistivity was then used to calculate the electrical conductivity using

$$\sigma = \frac{1}{\rho} \tag{4.2}$$

4.3 Angstrom Method for In-Plane Thermal Conductivity Measurement

The in-plane thermal transport properties of the printed epoxy/GnP composites were measured using the Angstrom method. This method is particularly useful for directionally structured materials because it measures thermal transport along the length of the sample rather than through the thickness. This is important for the present chapter because paste-extrusion-based 3D printing is expected to preferentially align graphene nanoplatelets along the print direction. Therefore, in-plane thermal diffusivity measured along the printed path provides a direct way to evaluate whether the printed filler structure improves directional heat transport.

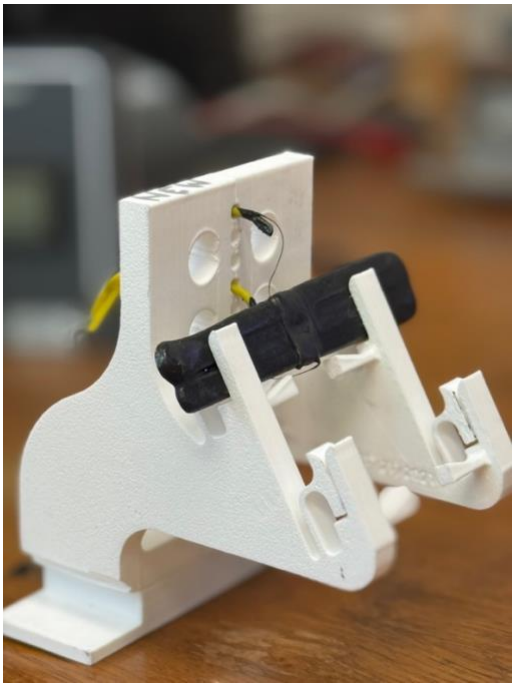


Figure 4.6 Sample holder for 3D printed samples

In this method, generally, a periodic heat input is applied to the sample and the resulting temperature wave is monitored at known distances from the heating location. In this work, a sinusoidal electrical heating was applied to a plane heater attached near the center of the printed sample. The generated heat wave propagated along the sample length, and the temperature response was recorded at multiple locations on the sample surface using an infrared thermal camera. Measurements were performed using sinusoidal heating conditions of 4 V peak-to-peak, +2V offset at 10 mHz frequency. The use of periodic heating allows the thermal diffusivity to be determined from the decay in temperature-wave amplitude and the phase lag between two measurement points. Figure 4.7 shows a screenshot of the FLIR software while running a measurement.

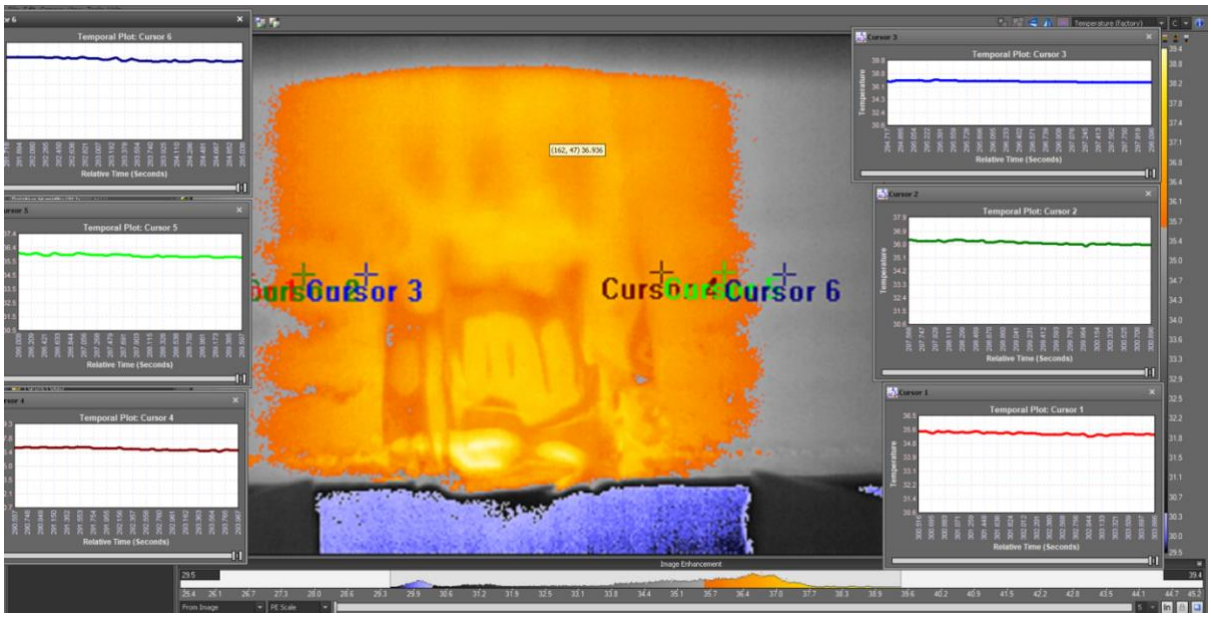


Figure 4.7 Screenshot of FLIR ResearchIR Max software during measurement

The figure shows 6 cursors used to collect the temperature at those points. The plots visible on either side of the cursors are the temporal plots corresponding to each of the 6 cursors. The

bright yellow-orange region visible in the thermal image corresponds to the high-temperature created by the heating wire, with the color intensity decreasing away from the heater as the thermal wave propagates through the printed sample. The temperature response at two points separated by a known distance, Δx, can be represented as two sinusoidal curves. The point farther from the heater has a lower amplitude and a delayed response compared to the point closer to the heater. The relevant quantities for the diffusivity calculation are the amplitude of the temperature wave at the first point, A_1, the amplitude of the temperature wave at the second point, A_2, the phase lag or time delay between the two temperature waves, Δt, and the physical distance between the two points, Δx. The thermal diffusivity, α, was calculated using the Angstrom relation,

$$\alpha = \frac{\Delta x^2}{2\Delta t \ln\left(\frac{A_1}{A_2}\right)} \tag{4.3}$$

The in-plane thermal conductivity was then calculated using

$$K = \alpha \, \rho \, C_p \tag{4.4}$$

where ρ is the density of the composite, and Cp is the specific heat capacity.

The measurement approach used in this work followed the infrared-camera-based Angstrom method developed previously in the laboratory [1]. In this approach, temperature is measured non-contact using an infrared camera instead of using thermocouples embedded into the sample. This reduces the need for drilling small holes or attaching thermocouples at each measurement location, which is especially useful for printed composite specimens that may be thin, fragile, or geometrically nonuniform. The infrared camera records the surface temperature

response during sinusoidal heating, and measurement points are selected digitally in the FLIR ResearchIR Max software.

A six-cursor method was used for temperature data extraction. Six measurement cursors were placed along the centerline of the sample at known distances from the heater. This arrangement provides three point pairs for calculating thermal diffusivity on both sides of the heater and allows the consistency of the measured temperature wave propagation to be checked along the sample. The cursor positions were determined from the sample geometry and camera image coordinates so that the distance between measurement points could be accurately related to the physical distance on the sample. This step is important because the Angstrom calculation is sensitive to Δx, and errors in cursor placement can directly affect the calculated diffusivity.

For each measurement, the sample was first allowed to reach a periodic steady response under sinusoidal heating. A representative section of the temperature-time data was then selected for analysis. The temperature response at each cursor was fit using a sinusoidal function to determine the amplitude and phase of the periodic temperature wave. The equation used for this fitting was

$$\theta(t) = Asin[\omega(t + C)] + B + Esin[2\omega(t + D)] \tag{4.5}$$

where $\theta(t)$ is fitted temperature at time t, A is the amplitude of the main sinusoidal temperature wave, ω is the angular frequency of heating, C is the phase/time shift of the main wave, B is the vertical offset, or average temperature, E is amplitude of the second harmonic term and D is the phase/time shift of the second harmonic. The amplitude ratio and phase lag between selected cursor pairs were then used to calculate the in-plane thermal diffusivity. Using multiple cursor pairs

allowed the calculated values to be compared within the same measurement, helping identify inconsistent data caused by local defects, nonuniform heating, poor surface quality, or weak temperature signal.

Several experimental factors can influence the accuracy of the Angstrom measurement. The sample should have a relatively constant width and thickness along the heat-flow direction so that the temperature wave is not affected by abrupt changes in geometry. Good contact between the plane heater and sample is also necessary to produce a stable and repeatable sinusoidal heat input. In addition, the surface observed by the infrared camera should have uniform emissivity so that measured temperature differences correspond to actual temperature variations rather than surface optical differences. For printed epoxy/GnP samples, surface roughness, voids, nonuniform filament geometry, and local filler-rich regions can introduce additional uncertainty.

The Angstrom method provides the in-plane thermal diffusivity along the direction of heat propagation. In this chapter, the measurement direction was selected to correspond to the print direction of the epoxy/GnP samples. Therefore, the measured thermal conductivity represents directional in-plane thermal conductivity along the printed path. This allows the effect of printing speed on directional thermal transport to be evaluated and related to print-induced graphene nanoplatelet alignment.

4.4 Results and Discussion

The effect of printing speed on the transport properties of printed epoxy/GnP composites was evaluated by comparing samples printed at 750, 1000, 1250, and 1500 mm/min. It is important to note here, that the extrusion values for each section of the sample was kept constant at all speeds.

Figure 4.8 shows the measured in-plane thermal conductivity and electrical conductivity of the printed composites as a function of printing speed. The thermal conductivity values represent heat transport along the printed direction, while the electrical conductivity values provide an additional indication of graphitic network formation within the printed composite.

Both thermal and electrical conductivity increased with increasing printing speed. The in-plane thermal conductivity increased from approximately 0.88 $Wm^{-1}K^{-1}$ at 750 mm/min to approximately 1.12 $Wm^{-1}K^{-1}$ at 1500 mm/min, corresponding to an increase of approximately 27%. A gradual increase was observed between 750 and 1250 mm/min, followed by a more significant increase at 1500 mm/min. A similar trend was observed for electrical conductivity, which increased from approximately 15.5 μS/cm at 750 mm/min to approximately 32 μS/cm at 1500 mm/min, corresponding to an increase of about 106%. The simultaneous increase in both thermal and electrical conductivity suggests that printing speed influenced the internal arrangement and connectivity of GnPs within the printed epoxy matrix.

The improvement in thermal conductivity with increasing printing speed may be related to changes in the flow and deposition behavior of the epoxy/GnP paste during extrusion. At higher printing speeds, the paste experiences different shear and deformation conditions during flow through the rectangular nozzle and during deposition onto the print bed. These conditions may promote greater preferential orientation of GnPs along the print direction, allowing heat to transfer more effectively through the high-conductivity in-plane direction of the nanoplatelets[103-106]. Since graphene nanoplatelets conduct heat much more efficiently along their basal plane than through their thickness direction, improved orientation along the print path can enhance directional in-plane thermal transport.

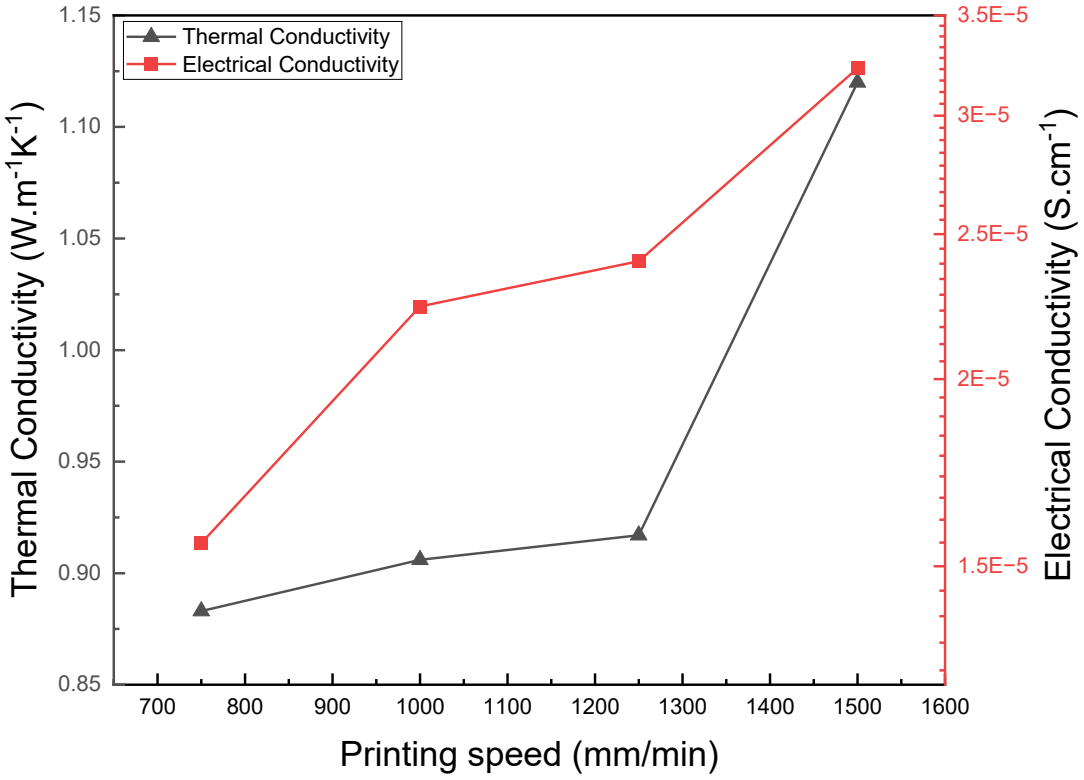


Figure 4.8 In-plane thermal and electrical conductivity of 3D printed epoxy/GnP sample

The corresponding increase in electrical conductivity also supports this interpretation. Electrical transport in epoxy/GnP composites depends strongly on the formation of connected graphitic pathways. The increase in electrical conductivity with printing speed indicates that the printed structure may contain more effective GnP-GnP contacts or a more continuous conductive network along the printed direction. Although electrical and thermal transport occur through different mechanisms, both properties are influenced by filler alignment, filler connectivity, and the continuity of the graphitic network[31,104,107-109]. Therefore, the similar increasing trends in thermal and electrical conductivity suggest that higher printing speeds improved the effectiveness of the GnP network in the printed composite.

The most significant improvement occurred between 1250 and 1500 mm/min. This indicates that the effect of printing speed was not completely linear over the tested range. At lower speeds, the changes in thermal conductivity were relatively small, suggesting that the GnP network and alignment state may have changed only gradually. At 1500 mm/min, however, the larger increase in both thermal and electrical conductivity suggests a stronger change in the printed microstructure. This may correspond to improved filler orientation, better continuity of the printed filament, or enhanced graphitic contact along the print direction.

4.5 Conclusion

In this chapter, paste-extrusion-based 3D printing was investigated as a processing route to improve directional transport properties in epoxy/graphene nanoplatelet composites. A 9wt% epoxy/GnP paste was prepared using acetone-assisted shear mixing and printed using a FELIX Food 1.6 single-head 3D printer. An 80 mm long rectangular nozzle with a 3 mm × 1.5 mm outlet was used for all printed samples, and the effect of printing speed was studied by comparing samples printed at 750, 1000, 1250, and 1500 mm/min. The printed samples were characterized for in-plane thermal conductivity along the print direction using the Angstrom method and for in-plane electrical conductivity using the four-probe method.

The in-plane thermal and electrical conductivities of the printed samples increased with increasing printing speed. Printing speed increase from 750 mm/min to 1500 mm/min resulted an increase of about 27% and 107% in thermal and electrical conductivity respectively. The similar increasing trends in thermal and electrical conductivity suggest that higher printing speeds improved the effectiveness of the GnP network along the printed direction.

These results show that printing speed is an important processing parameter for controlling directional transport in paste-extruded epoxy/GnP composites. Within the tested range, the highest printing speed of 1500 mm/min produced the highest in-plane thermal conductivity and electrical conductivity. This suggests that higher-speed printing can improve the utilization of GnP as a directional thermal filler, likely by modifying the flow-induced orientation and connectivity of the nanoplatelets. However, the final thermal performance is still expected to depend on the combined effects of filler alignment, filler-filler contact, void content, and printed filament quality.

Chapter 5

Conclusions

With rapid technological advances in electronics, electric vehicles, power systems, and compact energy devices, the demand for advanced thermal management materials continues to increase. In the context of this dissertation, emerging thermal management systems require materials that combine high thermal conductivity with low weight, durability, processability, and cost effectiveness. Metals are widely used in thermal management because of their high thermal conductivity and established manufacturing routes. However, their high density, susceptibility to corrosion, and limited suitability for some lightweight or complex composite systems create the need for alternative materials. Polymers are attractive candidates because they are lightweight, corrosion resistant, durable, and easy to process. The major limitation, however, is their low intrinsic thermal conductivity. To overcome this limitation, researchers have incorporated high thermal conductivity fillers such as metallic nanoparticles, carbon nanotubes, carbon nanowires, boron nitride platelets, graphene nanoplatelets, and expanded graphite into polymer matrices to form thermally conductive composites.

This dissertation focused on graphene nanoplatelets and expanded graphite as graphitic fillers in epoxy-based composites. Although graphene has very high intrinsic thermal conductivity, translating this property into high thermal conductivity epoxy composites is challenging. The effective thermal conductivity of these composites depends not only on the amount of filler added, but also on how the filler is organized inside the epoxy matrix. The three major challenges addressed in this dissertation were graphene nanoplatelet agglomeration, thermal resistance at

filler-polymer and filler-filler contacts, and inefficient use of graphene's anisotropic thermal conductivity due to random filler orientation. Therefore, the central objective of this dissertation was to improve thermal transport in epoxy/graphene-based composites by controlling filler dispersion, graphitic network connectivity, and filler alignment. Chapter 2 addressed dispersion through solvent-assisted processing, Chapter 3 addressed filler connectivity through expanded graphite, and Chapter 4 addressed filler orientation through paste-extrusion-based 3D printing. Together, these studies show that thermal conductivity enhancement is governed by the internal graphitic structure formed within the epoxy matrix, rather than by filler loading alone.

The first challenge addressed in this dissertation was the agglomeration of graphene nanoplatelets in epoxy. Graphene nanoplatelets have high thermal conductivity, but they tend to reaggregate during processing because of the strong van der Waals forces between the graphene sheets. This agglomeration leads to non-uniform filler dispersion in the epoxy matrix. As a result, some regions of the composite may contain large graphene-rich agglomerates, while other regions may have insufficient graphene to support thermal transport. This reduces the effective use of graphene as a high thermal conductivity filler. Chapter 2 investigated solvent-assisted processing as a method to improve graphene dispersion in epoxy composites. Two solvents, acetone and dimethylformamide (DMF), were compared for preparing epoxy/GnP composites. The results showed that solvent selection had a clear effect on the thermal conductivity of the composites, especially at higher graphene concentrations. At lower filler loading, the difference between acetone- and DMF-processed samples was limited. However, as the graphene loading increased, the DMF-processed composites showed higher thermal conductivity than the acetone-processed composites. At 7wt% graphene loading, the composite prepared using DMF showed 44% higher thermal conductivity than the composite prepared using acetone. This improvement was connected

to the better dispersion of graphene nanoplatelets in the DMF-processed samples. Confocal microscopy showed that acetone-based samples had larger graphene-rich agglomerates and a less uniform filler distribution. In comparison, the DMF-based samples showed a more uniform distribution of graphene throughout the epoxy matrix. Image analysis further confirmed that the maximum graphene agglomerate volume was higher in the acetone-based composites at higher filler loadings. This suggests that DMF was more effective in reducing graphene reaggregation during processing. Effective medium theory was also used to understand the effect of dispersion on thermal conductivity. The DMF-based composites showed lower apparent thermal interface resistance compared to the acetone-based composites. This does not mean that the local graphene-epoxy interface resistance was directly measured or completely removed. Instead, the apparent interface resistance should be understood as an effective transport parameter that includes the combined effects of graphene dispersion, agglomeration, graphene-epoxy contact, and the assumptions used in the model. Overall, Chapter 2 showed that improving filler dispersion can make the same graphene filler more effective in enhancing the thermal conductivity of epoxy composites.

The second challenge addressed in this dissertation was the limitation caused by filler-polymer and filler-filler contact resistance. Even if graphene nanoplatelets are well dispersed, heat transfer through the composite still requires heat to move through the epoxy matrix, through the graphitic fillers, and across many filler-filler junctions. These junctions can limit thermal transport because each contact between discrete particles can introduce thermal resistance. Therefore, improving the connectivity of graphitic fillers is important for obtaining higher thermal conductivity in epoxy-based composites. Chapter 3 investigated expanded graphite as a filler to improve graphitic network connectivity in epoxy. Expanded graphite was prepared using a H_2O_2/H_2SO_4-based

intercalation route followed by thermal expansion. The purpose of using expanded graphite was not to eliminate interface resistance completely, but to form more continuous graphitic pathways within the epoxy matrix. Compared with individual graphene nanoplatelets, expanded graphite can provide larger and more connected graphitic structures. This can reduce the dependence of thermal transport on many separate particle-particle contacts.

The epoxy/EG composites showed a significant increase in thermal conductivity with increasing EG loading up to 10wt%. The highest thermal conductivity obtained in this chapter was approximately 5.15 W m^{-1} K^{-1} at 10wt% EG. This result shows that H_2O_2-derived expanded graphite was effective in improving heat conduction through the epoxy matrix. The increase in thermal conductivity up to 10wt% suggests that the expanded graphite fillers formed more effective thermal pathways as the filler concentration increased. However, the results also showed that simply increasing filler loading does not always improve thermal conductivity. At higher filler loadings, such as 12.5 and 15wt%, the thermal conductivity decreased instead of continuing to increase. These samples showed poorer structural integrity compared with samples at lower filler concentrations. At these high filler loadings, the filler volume was substantially high, and the epoxy was not sufficient to compactly bond the fillers together. This likely weakened the quality of filler-filler contacts and filler-matrix bonding, which increased contact resistance and reduced thermal transport. Therefore, Chapter 3 showed that expanded graphite can improve epoxy thermal conductivity by forming more continuous graphitic networks, but this improvement depends on maintaining a good balance between filler loading and composite structural integrity. The best performance was obtained when the filler content was high enough to form effective graphitic pathways, but not so high that the epoxy matrix could no longer properly bind the filler network.

The third challenge addressed in this dissertation was the inefficient use of graphene's anisotropic thermal conductivity. Graphene has much higher thermal conductivity along its in-plane direction than through its thickness direction. Because of this, the orientation of graphene nanoplatelets inside the epoxy matrix plays an important role in the final thermal transport behavior. In randomly oriented composites, many nanoplatelets are not aligned with the desired heat flow direction, which limits the use of graphene's high in-plane thermal conductivity. Chapter 4 investigated paste-extrusion-based 3D printing as a method to induce graphene nanoplatelet alignment in epoxy composites. A 9wt% epoxy/GnP paste was prepared and printed using a rectangular nozzle. The rectangular nozzle was selected because it can impose confinement during extrusion and help form a flattened printed filament. During extrusion and deposition, the graphene nanoplatelets experience shear and flow along the nozzle and print path, which may promote alignment along the printing direction. The printed composites were studied using in-plane thermal measurements using the Angstrom method, and electrical conductivity measurements using the four-probe method. The Angstrom method was useful for this chapter because it measures in-plane thermal transport along the sample length. Since the printed samples were prepared along a defined print direction, this method allowed the directional thermal transport behavior of the printed epoxy/GnP composites to be evaluated. The results showed that increasing print speed improved the directional transport properties of the printed composites. As the print speed increased from 750 mm/min to 1500 mm/min, both in-plane thermal conductivity and electrical conductivity increased. The sample printed at 1500 mm/min showed the best performance among the tested speeds with 27% higher thermal conductivity and 106% higher electrical conductivity suggesting that higher print speed improved the effectiveness of the GnP network along the print direction.

Therefore, Chapter 4 showed that 3D printing can be used as a processing method to influence the internal filler structure of epoxy/GnP composites.

Note: AI-tools were used to improve the readability and review the document for grammatical correctness.

References

1 Wei, J., Vo, T. & Inam, F. Epoxy/graphene nanocomposites-processing and properties: A review. *RSC Advances* **5**, 73510-73524 (2015).

2 Papageorgiou, D. G., Kinloch, I. A. & Young, R. J. Mechanical properties of graphene and graphene-based nanocomposites. *Progress in Materials Science* **90**, 75-127 (2017).

3 Li, Z. *et al.* Control of the functionality of graphene oxide for its application in epoxy nanocomposites. *Polymer* **54**, 6437-6446 (2013).

4 Choy, C. L. Thermal conductivity of polymers. *Polymer* **18**, 984-1004 (1977).

5 Burger, N. *et al.* Review of thermal conductivity in composites: Mechanisms, parameters and theory. *Progress in Polymer Science* **61**, 1-28 (2016).

6 Han, Z. & Fina, A. Thermal conductivity of carbon nanotubes and their polymer nanocomposites: A review. *Progress in Polymer Science* **36**, 914-944 (2011).

7 Pop, E., Varshney, V. & Roy, A. K. Thermal properties of graphene: Fundamentals and applications. *MRS Bulletin* **37**, 1273-1281 (2012).

8 Su, Y., Li, J. J. & Weng, G. J. Theory of thermal conductivity of graphene-polymer nanocomposites with interfacial Kapitza resistance and graphene-graphene contact resistance. *Carbon* **137**, 222-233 (2018).

9 Sun, Y., Chen, L., Cui, L., Zhang, Y. & Du, X. Molecular dynamics simulation of the effect of oxygen-containing functional groups on the thermal conductivity of reduced graphene oxide. *Computational Materials Science* **148**, 176-183 (2018).

10 Yeom, Y. S. *et al.* Unprecedentedly high thermal conductivity of carbon/epoxy composites derived from parameter optimization studies. *Composites Science and Technology* **186**, 107915 (2020).

11 Balandin, A. A. & et al. Superior thermal conductivity of single-layer graphene. *Nano Letters* **8**, 902-907 (2008).

12 Ghosh, S. & et al. Extremely high thermal conductivity of graphene: Prospects for thermal management applications in nanoelectronic circuits. *Applied Physics Letters* **92**, 151911 (2008).

13 Tarannum, F. *et al.* Large Enhancement in Thermal Conductivity of Solvent− Cast Expanded Graphite/Polyetherimide Composites. *Nanomaterials* **12**, 1877 (2022).

14 Wei, B. & Yang, S. Polymer composites with expanded graphite network with superior thermal conductivity and electromagnetic interference shielding performance. *Chemical Engineering Journal* **404**, 126437 (2021).

15 Liu, C. & et al. 3D expanded graphite frameworks for dual-functional polymer composites with exceptional thermal conductive and electromagnetic interference shielding capabilities. *ACS Applied Electronic Materials* **4**, 707-717 (2022).

16 Wang, F., Drzal, L. T., Qin, Y. & Huang, Z. Mechanical properties and thermal conductivity of graphene nanoplatelet/epoxy composites. *Journal of Materials Science* **50**, 1082-1093 (2015).

17 Han, S. *et al.* Mechanical, toughness and thermal properties of 2D material-reinforced epoxy composites. *Polymer* **184**, 121884 (2019).

18 Guo, W. & Chen, G. Fabrication of graphene/epoxy resin composites with much enhanced thermal conductivity via ball milling technique. *Journal of Applied Polymer Science* **131** (2014).

19 Nan, C. W., Birringer, R., Clarke, D. R. & Gleiter, H. Effective thermal conductivity of particulate composites with interfacial thermal resistance. *Journal of Applied Physics* **81**, 6692-6699 (1997).

20 Tang, L. C. *et al.* The effect of graphene dispersion on the mechanical properties of graphene/epoxy composites. *Carbon* **60**, 16-27 (2013).

21 Wei, J., Saharudin, M. S., Vo, T. & Inam, F. N,N-Dimethylformamide (DMF) usage in epoxy/graphene nanocomposites: Problems associated with reaggregation. *Polymers* **9**, 193 (2017).

22 Villar-Rodil, S., Paredes, J. I., Martínez-Alonso, A. & Tascón, J. M. Preparation of graphene dispersions and graphene-polymer composites in organic media. *Journal of Materials Chemistry* **19**, 3591-3593 (2009).

23 Huxtable, S. T. & et al. Interfacial heat flow in carbon nanotube suspensions. *Nature Materials* **2**, 731-734 (2003).

24 Shenogin, S., Xue, L., Ozisik, R., Keblinski, P. & Cahill, D. G. Role of thermal boundary resistance on the heat flow in carbon-nanotube composites. *Journal of Applied Physics* **95**, 8136-8144 (2004).

25 Konatham, D. & Striolo, A. Thermal boundary resistance at the graphene-oil interface. *Applied Physics Letters* **95**, 163105 (2009).

26 Nika, D. L. & Balandin, A. A. Phonons and thermal transport in graphene and graphene-based materials. *Reports on Progress in Physics* **80**, 036502 (2017).

27 Lindsay, L., Broido, D. A. & Mingo, N. Flexural phonons and thermal transport in graphene. *Physical Review B* **82**, 115427 (2010).

28 Li, A., Zhang, C. & Zhang, Y. F. Thermal Conductivity of Graphene-Polymer Composites: Mechanisms, Properties, and Applications. *Polymers (Basel)* **9**, 437 (2017). https://doi.org/10.3390/polym9090437

29 Shtein, M., Nadiv, R., Buzaglo, M., Kahil, K. & Regev, O. Thermally conductive graphene-polymer composites: size, percolation, and synergy effects. *Chemistry of Materials* **27**, 2100-2106 (2015).

30 Tarannum, F. *et al.* Hydrogen-peroxide intercalated expanded graphite facilitates large enhancement in thermal conductivity of polyetherimide/graphite nanocomposites. *Journal of Materials Research and Technology* **33**, 1420-1435 (2024).

31 Tarannum, F. *et al.* Thermally expanded graphite polyetherimide composite with superior electrical and thermal conductivity. *Materials Chemistry and Physics* **298**, 127404 (2023).

32 Wu, Y. & et al. 3D printed graphene and graphene/polymer composites for multiple applications. *Composites Part A: Applied Science and Manufacturing* **167**, 107405 (2023).

33 Balandin, A. A. Thermal properties of graphene and nanostructured carbon materials. *Nature materials* **10**, 569-581 (2011).

34 Novoselov, K. S. *et al.* Electric field effect in atomically thin carbon films. *Science* **306**, 666-669 (2004).

35 Galpaya, D. *et al.* Preparation of graphene oxide/epoxy nanocomposites with significantly improved mechanical properties. *Journal of Applied Physics* **116**, 053518 (2014).

36 Paredes, J., Villar-Rodil, S., Martínez-Alonso, A. & Tascon, J. Graphene oxide dispersions in organic solvents. *Langmuir* **24**, 10560-10564 (2008).

37 Mishra, K., Babu, L. K., Dhakal, D., Lamichhane, P. & Vaidyanathan, R. K. The effect of solvent on the mechanical properties of polyhedral oligomeric silsesquioxane (POSS)–epoxy nanocomposites. *SN Applied Sciences* **1**, 1-7 (2019).

38 Wang, F., Drzal, L. T., Qin, Y. & Huang, Z. Mechanical properties and thermal conductivity of graphene nanoplatelet/epoxy composites. *Journal of materials science* **50**, 1082-1093 (2015).

39 Guo, W. & Chen, G. Fabrication of graphene/epoxy resin composites with much enhanced thermal conductivity via ball milling technique. *Journal of Applied Polymer Science* **131** (2014).

40 Hansen, C. M. *Hansen solubility parameters: a user's handbook*. (CRC press, 2007).

41 Hernandez, Y. *et al.* High-yield production of graphene by liquid-phase exfoliation of graphite. *Nature Nanotechnology* **3**, 563-568 (2008). https://doi.org/10.1038/nnano.2008.215

42 Park, S. *et al.* Colloidal suspensions of highly reduced graphene oxide in a wide variety of organic solvents. *Nano letters* **9**, 1593-1597 (2009).

43 Hernandez, Y., Lotya, M., Rickard, D., Bergin, S. D. & Coleman, J. N. Measurement of multicomponent solubility parameters for graphene facilitates solvent discovery. *Langmuir* **26**, 3208-3213 (2010).

44 Kulkarni, V. S. *Handbook of non-invasive drug delivery systems: science and technology*. (Elsevier, 2009).

45 Hunter, R. J. *Zeta Potential in Colloid Science: Principles and Applications*. (Academic Press, 1981).

46 Bhattacharjee, S. DLS and zeta potential - What they are and what they are not? *Journal of Controlled Release* **235**, 337-351 (2016). https://doi.org/10.1016/j.jconrel.2016.06.017

47 Grumezescu, A. M. *Nanomaterials for drug delivery and therapy*. (William Andrew, 2019).

48 Ghazvini, A. S. *et al.* Co-electrophoretic deposition of Co3O4 and graphene nanoplates for supercapacitor electrode. *Materials Letters* **285**, 129195 (2021).

49 Gambhir, S., Murray, E., Sayyar, S., Wallace, G. G. & Officer, D. L. Anhydrous organic dispersions of highly reduced chemically converted graphene. *Carbon* **76**, 368-377 (2014).

50 Villar-Rodil, S., Paredes, J. I., Martínez-Alonso, A. & Tascón, J. M. Preparation of graphene dispersions and graphene-polymer composites in organic media. *Journal of Materials Chemistry* **19**, 3591-3593 (2009).

51 Tarannum, F., Muthaiah, R., Annam, R. S., Gu, T. & Garg, J. Effect of alignment on enhancement of thermal conductivity of polyethylene-graphene nanocomposites and comparison with effective medium theory. *Nanomaterials* **10**, 1291 (2020).

52 Saeidijavash, M. *et al.* High thermal conductivity through simultaneously aligned polyethylene lamellae and graphene nanoplatelets. *Nanoscale* **9**, 12867-12873 (2017).

53 Wilson, T. & Carlini, A. Three-dimensional imaging in confocal imaging systems with finite sized detectors. *Journal of Microscopy* **149**, 51-66 (1988).

54 Srinivas, K. & Bhagyashekar, M. S. Thermal conductivity enhancement of epoxy by hybrid particulate fillers of graphite and silicon carbide. *Journal of Minerals and Materials Characterization and Engineering* **3**, 76 (2015).

55 Li, M. & Mu, B. Effect of different dimensional carbon materials on the properties and application of phase change materials: A review. *Applied Energy* **242**, 695-715 (2019).

56 Li, A., Zhang, C. & Zhang, Y. F. Thermal conductivity of graphene-polymer composites: Mechanisms, properties, and applications. *Polymers* **9**, 437 (2017).

57 Isarn, I., Bonnaud, L., Massagues, L., Serra, A. & Ferrando, F. Enhancement of thermal conductivity in epoxy coatings through the combined addition of expanded graphite and boron nitride fillers. *Progress in Organic Coatings* **133**, 299-308 (2019).

58 Yim, Y.-J. & Park, S.-J. Effect of silver-plated expanded graphite addition on thermal and electrical conductivities of epoxy composites in the presence of graphite and copper. *Composites Part A: Applied Science and Manufacturing* **123**, 253-259 (2019).

59 Wang, Z., Qi, R., Wang, J. & Qi, S. Thermal conductivity improvement of epoxy composite filled with expanded graphite. *Ceramics International* **41**, 13541-13546 (2015).

60 Jin, F.-L., Chu, N., Yao, S.-S. & Park, S.-J. Thermal and electrical conductivity improvement in epoxy resin with expanded graphite and silver plating. *Korean Journal of Chemical Engineering* **39**, 2182-2191 (2022).

61 Kumar, R., Mohanty, S. & Nayak, S. K. Study on epoxy resin-based thermal adhesive filled with hybrid expanded graphite and graphene nanoplatelet. *SN Applied Sciences* **1**, 1-13 (2019).

62 Lin, X., Zhang, X., Liu, L., Liang, J. & Liu, W. Polymer/expanded graphite-based flexible phase change material with high thermal conductivity for battery thermal management. *Journal of Cleaner Production* **331**, 130014 (2022).

63 Tao, Z., Wang, H., Li, X., Liu, Z. & Guo, Q. Expanded graphite/polydimethylsiloxane composites with high thermal conductivity. *Journal of Applied Polymer Science* **134** (2017).

64 Danayat, S. S., Mona, Z., Avinash, N., Annam, R. S. & Garg, J. Role of four-phonon processes in thermal conductivity of two-dimensional materials and thermal-transport enhancement arising from interconnected nanofiller networks in polymer/nanofiller composites. *Nanoscale* (2024).

65 Wei, Q. & et al. High-performance expanded graphite from flake graphite by microwave-assisted chemical intercalation process. *Journal of Industrial and Engineering Chemistry* **122**, 562-572 (2023).

66 Chen, Y. P., Li, S. Y., Luo, R. Y., Lv, X. M. & Wang, X. J. Optimization of initial redox potential in the preparation of expandable graphite by chemical oxidation. *New Carbon Materials* **28**, 435-441 (2013).

67 Goudarzi, R. & Motlagh, G. H. The effect of graphite intercalated compound particle size and exfoliation temperature on porosity and macromolecular diffusion in expanded graphite. *Heliyon* **5** (2019).

68 Trivedi, A., Pisharath, N. & Ramanujam, B. Effect of oxidizing agents on the expansion characteristics of natural graphite. *Materials Today: Proceedings* **5**, 16695-16702 (2018).

69 Muthaiah, R. & Garg, J. Thermal conductivity of magnesium selenide (MgSe)–A first principles study. *Computational Materials Science* **198**, 110679 (2021).

70 Kim, Y. *et al.* Breakdown of the interlayer coherence in twisted bilayer graphene. *Physical Review Letters* **110**, 096602 (2013).

71 Cai, M., Thorpe, D., Adamson, D. H. & Schniepp, H. C. Methods of graphite exfoliation. *Journal of Materials Chemistry* **22**, 24992-25002 (2012).

72 Noel, M. & Santhanam, R. Electrochemistry of graphite intercalation compounds. *Journal of Power Sources* **72**, 53-65 (1998).

73 Wang, Y. *et al.* Enhanced thermal and electrical properties of epoxy composites reinforced with graphene nanoplatelets. *Polymer Composites* **36**, 556-565 (2015).

74 Van Heerden, X. & Badenhorst, H. The influence of three different intercalation techniques on the microstructure of exfoliated graphite. *Carbon* **88**, 173-184 (2015).

75 Rüdorff, W. Kristallstruktur der saeureverbindungen des graphits. *Zeitschrift für Physikalische Chemie* **45**, 42-68 (1940).

76 Yakovlev, A., Finaenov, A., Zabud'Kov, S. & Yakovleva, E. Thermally expanded graphite: Synthesis, properties, and prospects for use. *Russian journal of applied chemistry* **79**, 1741-1751 (2006).

77 Xia, Z., Bellani, V., Sun, J. & Palermo, V. Electrochemical exfoliation of graphite in H 2 SO 4, Li 2 SO 4 and NaClO 4 solutions monitored in situ by Raman microscopy and spectroscopy. *Faraday Discussions* **227**, 291-305 (2021).

78 Yu, P., Lowe, S. E., Simon, G. P. & Zhong, Y. L. Electrochemical exfoliation of graphite and production of functional graphene. *Current opinion in colloid & interface science* **20**, 329-338 (2015).

79 Su, C.-Y. *et al.* High-quality thin graphene films from fast electrochemical exfoliation. *ACS nano* **5**, 2332-2339 (2011).

80 Wang, Z. & et al. A roadmap review of thermally conductive polymer composites: critical factors, progress, and prospects. *Advanced Functional Materials* **33**, 2301549 (2023).

81 Chen, J., Xu, X., Zhou, J. & Li, B. Interfacial thermal resistance: Past, present, and future. *Reviews of Modern Physics* **94**, 025002 (2022).

82 Jasmee, S., Omar, G., Othaman, S. S. C., Masripan, N. A. & A. Hamid, H. Interface thermal resistance and thermal conductivity of polymer composites at different types, shapes, and sizes of fillers: A review. *Polymer Composites* **42**, 2629-2652 (2021).

83 Guo, Y., Ruan, K. & Gu, J. Controllable thermal conductivity in composites by constructing thermal conduction networks. *Materials Today Physics* **20**, 100449 (2021).

84 Zha, J. W., Wang, F. & Wan, B. Polymer composites with high thermal conductivity: Theory, simulation, structure and interfacial regulation. *Progress in Materials Science* **148**, 101362 (2025).

85 Ruan, K., Shi, X., Guo, Y. & Gu, J. Interfacial thermal resistance in thermally conductive polymer composites: a review. *Composites Communications* **22**, 100518 (2020).

86 Ferrari, A. C. & Basko, D. M. Raman spectroscopy as a versatile tool for studying the properties of graphene. *Nature Nanotechnology* **8**, 235-246 (2013).

87 Ferrari, A. C. & et al. Raman spectrum of graphene and graphene layers. *Physical Review Letters* **97**, 187401 (2006).

88 Cancado, L. G. & et al. Quantifying defects in graphene via Raman spectroscopy at different excitation energies. *Nano Letters* **11**, 3190-3196 (2011).

89 Zhao, W. & et al. Defect-engineered heat transport in graphene: a route to high efficient thermal rectification. *Scientific Reports* **5**, 11962 (2015).

90 Malekpour, H. & et al. Thermal conductivity of graphene with defects induced by electron beam irradiation. *Nanoscale* **8**, 14608-14616 (2016).

91 Naebe, M. & et al. Mechanical property and structure of covalent functionalised graphene/epoxy nanocomposites. *Scientific Reports* **4**, 4375 (2014).

92 Bao, D. & et al. A novel modified expanded graphite/epoxy 3D composite with ultrahigh thermal conductivity. *Chemical Engineering Journal* **433**, 133519 (2022).

93 Xia, L., Zhang, P. & Wang, R. Preparation and thermal characterization of expanded graphite/paraffin composite phase change material. *Carbon* **48**, 2538-2548 (2010).

94 You, X., Zhang, Q., Yang, J. & Dong, S. Review on 3D-printed graphene-reinforced composites for structural applications. *Composites Part A: Applied Science and Manufacturing* **167**, 107420 (2023).

95 Guo, H., Lv, R. & Bai, S. Recent advances on 3D printing graphene-based composites. *Nano Materials Science* **1**, 101-115 (2019).

96 You, X., Yang, J. & Dong, S. Structural and functional applications of 3D-printed graphene-based architectures. *Journal of Materials Science* **56**, 9007-9046 (2021).

97 Du, J., Fu, G., Xu, X., Elshahawy, A. M. & Guan, C. 3D printed graphene-based metamaterials: guesting multi-functionality in one gain. *Small* **19**, 2207833 (2023).

98 Wang, J. *et al.* Ink-based 3D printing technologies for graphene-based materials: a review. *Advanced composites and hybrid materials* **2**, 1-33 (2019).

99 Friedrich, L. & Begley, M. in *Polymer-Based Additive Manufacturing: Recent Developments* 131-149 (ACS Publications, 2019).

100 Jang, S. *et al.* Effect of material extrusion process parameters on filament geometry and inter-filament voids in as-fabricated high solids loaded polymer composites. *Additive Manufacturing* **47**, 102313 (2021).

101 Walton, R. L. *et al.* Direct writing of textured ceramics using anisotropic nozzles. *Journal of the European Ceramic Society* **41**, 1945-1953 (2021).

102 Marnot, A., Dobbs, A. & Brettmann, B. Material extrusion additive manufacturing of dense pastes consisting of macroscopic particles. *MRS communications* **12**, 483-494 (2022).

103 Xiao, B. *et al.* Controlling shear rate for designable thermal conductivity in direct ink printing of polydimethylsiloxane/boron nitride composites. *Polymers* **15**, 3489 (2023).

104 Haney, R. *et al.* Printability and performance of 3D conductive graphite structures. *Additive Manufacturing* **37**, 101618 (2021).

105 Wang, Z. *et al.* Fused deposition modeling of isotactic polypropylene/graphene nanoplatelets composites: achieving enhanced thermal conductivity through filler orientation. *Polymers* **16**, 772 (2024).

106 Guo, H. *et al.* Highly thermally conductive 3D printed graphene filled polymer composites for scalable thermal management applications. *Acs Nano* **15**, 6917-6928 (2021).

107 Chen, J. & Gao, X. Directional dependence of electrical and thermal properties in graphene-nanoplatelet-based composite materials. *Results in Physics* **15**, 102608 (2019).

108 Wu, S. *et al.* Aligning multilayer graphene flakes with an external electric field to improve multifunctional properties of epoxy nanocomposites. *Carbon* **94**, 607-618 (2015).

109 Tian, X., Itkis, M. E., Bekyarova, E. B. & Haddon, R. C. Anisotropic thermal and electrical properties of thin thermal interface layers of graphite nanoplatelet-based composites. *Scientific reports* **3**, 1710 (2013).